

Chapter 2

Quantum Interference and Superposition

2.1 Introduction

One of the methods that we have to probe and explore the quantum world is by means of scattering experiments. When particles collide, and the outcome from these collisions provides us with information about the nature of such particles and their interactions. From a fundamental point of view, it was the diffracted pattern formed by the scattered particles what led Born to establish the statistical interpretation of quantum mechanics and de Broglie to confirm his wave-corpuscle hypothesis. This behavior was first observed experimentally by Davisson and Germer in 1927 [1, 2], who showed that electrons have wave properties by observing how a beam of thermally excited electrons got diffracted by a nickel crystal at larger angles than predicted by the classical laws of motion. After this experiment with electrons, in the 1930s Stern and coworkers [3–5] showed molecular hydrogen diffraction by surfaces. Many other experiments followed with different types of particles, like electrons [6–14], slow neutrons [15, 16], atoms [17–20], small atomic clusters [21], very large molecules [22–25] and even Bose-Einstein condensates [26], giving rise to modern matter-wave interferometry.

In all these cases (which constitute just a brief overview of the very large number of experiments carried out since 1927), high intensity beams, i.e., a large flux of particles, are used to show the wave-like property of matter. However, more recently, low intensity beams have also been used to show that even single particles, like photons [27–30], electrons [10, 13, 14] or sodium atoms [31], when collected one by one and after a relatively long time, will reproduce the results expected by quantum mechanics. These results not only constitute a physical demonstration of Born’s statistical interpretation, but also lead us to rethink and understand quantum mechanics from a different perspective, namely in terms of a real-time dynamics (see Chap. 6, Vol. 1).

Now, in order to better contextualize the relevance of quantum interference, it is unavoidable to pass through the concept of *quantum entanglement* [32–35]. Approximately, in these last 15 years, the fields of quantum information theory [36, 37],

quantum computation [36, 37] and quantum control have undergone a fast development. Due to the relevant role played by entanglement in all these fields, the idea that this phenomenon is the most distinctive feature of quantum mechanics has also grown in importance, something that we can already see in Schrödinger's 1935 statement [32]:

When two systems, of which we know the states by their respective representatives, enter into temporary physical interaction due to known forces between them, and when after a time of mutual influence the systems separate again, then they can no longer be described in the same way, viz. by endowing each of them with a representative of its own. I would not call that *one* but rather *the* characteristic trait of quantum mechanics, the one that enforces its entire departure from classical lines of thought. By the interaction the two representatives (or ψ -functions) have become entangled.

Even though, *interference* is a still more fundamental feature of quantum mechanics. The most striking manifestation of this phenomenon is, most surely, Young's celebrated two-slit experiment; quoting Feynman [38], this experiment "has in it the heart of quantum mechanics. In reality, it contains the *only* mystery." Quantum interference is a direct consequence of the *coherent* superposition of (quantum) probability fields, just as in classical wave mechanics interference arises from the coherent superposition of energy fields. However, what is special about quantum interference (with respect to its classical counterpart) is the fact that it is associated with a nonphysical quantity, namely the single-particle probability distribution—remember that classical waves are a manifestation of the transmission of energy (a physical magnitude) throughout a perturbed medium. Of course, when more than one particle interact, the corresponding multi-particle coherent superpositions are necessarily described by nonfactorizable or entangled states, which give rise to interesting (multi-particle) interference processes (as seen, for instance, in two-particle coincidence experiments or EPR-like experiments).

Quantum interference is not only important at a conceptual and fundamental level, but also from a practical point of view due to the very wide range of experimental situations and applications where it is involved. SQUIDs or superconducting quantum interference devices [39] constitute one of the relevant fields where interference plays a fundamental role, but also in experiments based on coherence control [40], where interference mechanisms are considered in order to enhance or inhibit the formation of products in chemical reactions. Another actual research field where interference is very important is atom and molecular interferometry [41], in particular, with Bose-Einstein condensates [42–44], where different techniques to recombine the split beams are used [45–50]. Also, the experimental realization of the Talbot effect with relatively heavy particles (e.g., Na atoms [51] and Bose-Einstein condensates [52]), which is not merely a two-slit-like interference process, but an interesting case of multi-interference. Finally, it is important to mention that the theoretical grounds of the quantum information theory (and quantum computation) also rely on the idea of a coherent superposition: the *qubit* [37]. The unit of classical information is the *bit*, which can have one out of two possible outcomes, 0 or 1, according to the most standard binary notation. The quantum-mechanical analogs are the special orthonormal basis states $|0\rangle$ and $|1\rangle$, known as *computational basis*

states. However, contrary to the classical case, in quantum mechanics an infinity of possible outcomes or states can be assigned to a qubit. This can be represented, in general, as a coherent superposition

$$|\psi\rangle = \cos(\theta/2)|0\rangle + e^{i\phi} \sin(\theta/2)|1\rangle, \quad (2.1)$$

where θ and ϕ define one of the infinite points covering the surface of a unit sphere, namely the *Bloch sphere*—on this sphere, $|0\rangle$ and $|1\rangle$ point in the opposite directions. The possibility to encode information in superpositions like (2.1) already gives an idea of the actual interest in the quantum information theory and quantum computation.

The examples given above constitute just a small sample of the many cases where interference is important. Now, there is a “weakness” in the interpretation of interference phenomena: as also taught in classical wave mechanics courses, due to the superposition principle the flows associated with two interfering waves (regardless of what these waves may represent, either energy or probability fluxes) are uncorrelated. When proceeding in this way, some kind of reality is associated with the superposition principle. However, in Nature waves cannot be decomposed and then added up again, but they and their effects always appear as a whole, independently of whether the corresponding phenomenon is classical or quantum-mechanical. The purpose of this chapter is precisely to address this issue with the aid of Bohmian mechanics and a simple two Gaussian wave-packet superposition. Notice that, actually, rather than being simple academical examples, such superpositions are shown to be experimentally realizable (and, indeed, used) in atom interferometry [45–50]. In Fig. 2.1, for instance, we have sketched two types of experiments where coherent superpositions of Gaussian wave packets can be produced. Accordingly, we have organized this chapter as follows. In next section, we analyze the superposition principle from a dynamical viewpoint, using as a tool Bohmian mechanics. In Sect. 2.3 the implications of the Bohmian non-crossing rule are studied, while in Sect. 2.4 the similarities with collision problems are discussed. The extension of quantum interference effects to a complex configuration space is introduced in Sect. 2.5. Different aspects of Young’s two-slit experiment are described in Sect. 2.6. Finally, the effects of dissipative and stochastic dynamics are considered in Sects. 2.7 and 2.8, respectively.

2.2 Superposition Principle and Interference Dynamics

As any wave equation, the time-dependent Schrödinger equation is also linear in the field variable, Ψ , and therefore satisfies the *superposition principle*. Within this context, this means that any wave function solution of this equation can be linearly decomposed (at any time) as a sum of a series of other solutions of the same equation (for the same potential function),

$$\Psi(\mathbf{r}, t) = \sum_{i=1}^N c_i \psi_i(\mathbf{r}, t), \quad (2.2)$$

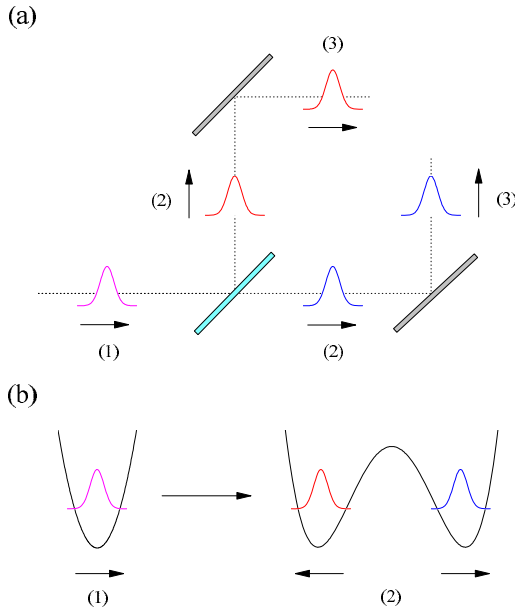


Fig. 2.1 Two situations where the wave function describing the system can be described in terms of a two-wave-packet superposition. **(a)** After reaching a beam-splitter, an incoming wave packet (1) splits into two wave packets (2). These wave packets move apart until they reach two reflectance mirrors, which redirect their propagation (3) in such a way that, after some time, they will “collide”, displaying interference. **(b)** A wave packet confined in a potential well (1) is split into two wave packets by creating a barrier inside the potential (2) and then pulling outwards the two new potential wells (each containing a new wave packet). After these wave packets are separated, the potential can be turned off and then control the propagation of such wave packets to make them to interfere, as happens in Bose-Einstein interferometric techniques

This is a *coherent* sum, which gives rise to interference phenomena (see Sect. 4.3, in Vol. 1) whenever two or more of these components overlap, i.e., coincide spatially at a given time. Mathematically, the superposition principle facilitates the obtention of solutions of the Schrödinger equation, since complex solutions can be found in terms of simpler ones—e.g., scattering wave functions can be obtained from linear combinations of plane waves, or the evolution of wave packets in bound potentials from the superposition of the eigenstates for this potential. However, from a physical point of view, assuming a hydrodynamical picture, a quantum system does not display the same behavior when it is represented by the total solution Ψ than when the same is done by means of each partial one, ψ_i , separately. This is actually a crucial point to understand in simple terms (i.e., without appealing to any decoherence source) puzzling behaviors, such as quantum complementarity.

In order to get a glimpse of the meaning of the previous statement, consider the superposition of two counter-propagating Gaussian wave packets in one dimension. Though simple, this model contains in it the essential ingredients to obtain a full understanding of the physics involved in the superposition principle, and eventually

the two-slit experiment and quantum interference phenomena. Thus, such a superposition is described by

$$\Psi(x, t) = c_1\psi_1(x, t) + c_2\psi_2(x, t), \quad (2.3)$$

where the partial waves ψ_i are normalized Gaussian wave packets, as (1.2). These wave packets propagate with opposite velocities, with modulus $|v_t| = |p_t|/m$, and are initially far enough to ensure a vanishing overlapping between them, i.e., $\rho_1(x, 0)\rho_2(x, 0) \approx 0$ (hence the weighting factors c_1 and c_2 can be chosen such that $|c_1|^2 + |c_2|^2 \approx 1$). Accordingly, there should not be any sort of physical relation between the wave packets, except when they approach and interference features emerge. However, when we appeal to the total phase of (2.3), $S(x, t) = (\hbar/2i) \ln(\Psi/\Psi^*)$, and the associated velocity field,

$$v(x, t) = \dot{x} = \frac{\hbar}{2mi} \frac{\Psi^* \nabla \Psi - \Psi \nabla \Psi^*}{\Psi \Psi^*}, \quad (2.4)$$

a different picture arises. This becomes more apparent by inspection of Fig. 2.2. Here, the Bohmian trajectories obtained after numerical integration of (2.4) are represented (white solid lines) together with the space-time contour plots of the probability density ρ (a), phase S (b) and velocity v (c) fields associated with Ψ . As seen in panel (a), initially we have two separated wave packets and therefore two swarms of trajectories which seem to be uncorrelated. However, if we have a look at panels (b) and (c), we notice that the situation is very different: because the wave packets are *coherent*, i.e., both are present at the same time, there is a phase effect which makes the trajectories associated with one of these wave packets to know about the existence of the other, and vice versa. Due to this fact, when interference features start developing, it is not only that the incipient nodes of the wave function lead the trajectories to display wiggling paths to avoid them, but there are important phase effects which do not allow the trajectories coming from one wave packet entering the domain of those coming from the other. Note that the phase field as well as the velocity field consist of two well-defined domains, this picture being very different from the one that we would have (one single domain covering the whole configuration space) if only one of the two wave packets was present at a time. By inspection of the velocity field, for example, we observe that one of the regions is initially characterized by forward motion (positive local velocities, denoted by the yellowish in the contour plot) and the other by backward motion (negative local velocities, with blueish in the contour plot) separated by a sort of “interface” at $x = 0$ that acts like a fictitious infinite barrier. As interference becomes apparent, a series of alternating bands of opposite colors appear, which imply that in regions of forward motion one also can find backward one, and vice versa, this being the cause of the wiggles in the trajectories. When interference reaches its maximum, a phase-transition is observed: the region of forward motion becomes a backward

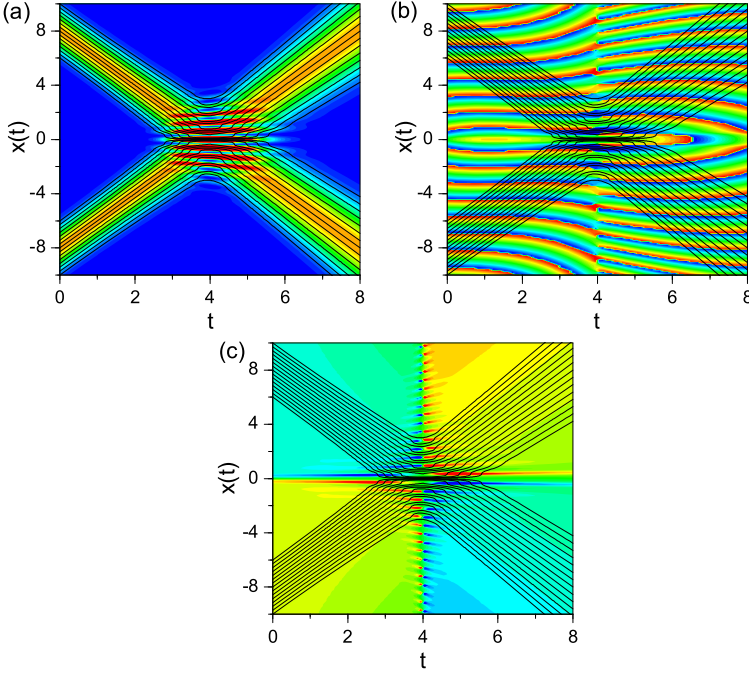


Fig. 2.2 Space-time contour plots of the probability density (a), phase field (b), and velocity field (c) for a coherent superposition of two counter-propagating Gaussian wave packets, with $v_0 \gg v_s$. From darker (*blue*) to lighter (*red*) contours, increasing values of the corresponding fields; the *black solid lines* correspond to Bohmian trajectories starting at different initial positions. The numerical parameters considered in the simulation are: $\sigma_0 = 1$, $x_0^{(i)} = \mp 8$, $v_0^{(i)} = \pm 2$ (with $i = 1, 2$) and $m = 1$

motion one, and vice versa, which makes the trajectories to display a sort of bounce backwards.

The previous statement can be formally justified. As seen in Sect. 1.2, depending on the ratio between v_0 and v_s (let us assume that $|x_0| \approx \sigma_0$), one finds that the asymptotic motion can be either essentially classical (negligible spreading compared to the distances traveled by the wave packet) or purely quantum mechanical (if v_s dominates and therefore the wave-packet spreading is much more relevant than the traveled distance). Within the present context, this translates into two possible situations [53]: collision-like ($v_0 \gg v_s$) and diffraction-like ($v_0 \ll v_s$). In the first case, interference is localized in time within a certain spatial region (as in Fig. 2.2) and the asymptotic output is just two well-defined wave packets moving apart from each other. In the second case, interference features persist in time once they have developed, giving rise to a situation similar to that of a two-slit experiment.

Having said that, let us recast (2.3) in the more convenient form

$$\Psi = c_1(\psi_1 + \sqrt{\alpha}\psi_2), \quad (2.5)$$

where $\alpha = (c_2/c_1)^2$ (with $c_1 \neq 0$). Accordingly, the probability density and the quantum current density read as

$$\rho = c_1^2 [\rho_1 + \alpha \rho_2 + 2\sqrt{\alpha} \sqrt{\rho_1 \rho_2} \cos \varphi], \quad (2.6)$$

$$\begin{aligned} \mathbf{J} = \frac{c_1^2}{m} & [\rho_1 \nabla S_1 + \alpha \rho_2 \nabla S_2 + \sqrt{\alpha} \sqrt{\rho_1 \rho_2} \nabla (S_1 + S_2) \cos \varphi \\ & + \hbar \sqrt{\alpha} (\rho_1^{1/2} \nabla \rho_2^{1/2} - \rho_2^{1/2} \nabla \rho_1^{1/2}) \sin \varphi], \end{aligned} \quad (2.7)$$

respectively (the vector notation for the quantum current density is chosen to stress the fact that, in general, this quantity is a vector, even though here we are considering one dimension). The corresponding Bohmian trajectories are obtained after substituting these two quantities into the “guidance equation”,

$$\begin{aligned} \dot{\mathbf{r}} = \frac{\mathbf{J}}{\rho} = \frac{1}{m} & \frac{\rho_1 \nabla S_1 + \alpha \rho_2 \nabla S_2 + \sqrt{\alpha} \sqrt{\rho_1 \rho_2} \nabla (S_1 + S_2) \cos \varphi}{\rho_1 + \alpha \rho_2 + 2\sqrt{\alpha} \sqrt{\rho_1 \rho_2} \cos \varphi} \\ & + \sqrt{\alpha} \frac{\hbar (\rho_1^{1/2} \nabla \rho_2^{1/2} - \rho_2^{1/2} \nabla \rho_1^{1/2}) \sin \varphi}{\rho_1 + \alpha \rho_2 + 2\sqrt{\alpha} \sqrt{\rho_1 \rho_2} \cos \varphi}. \end{aligned} \quad (2.8)$$

In this latter expression, we notice two well-defined contributions related to the effects that the interchange of the wave packets has on particle motion after interference (specifically, on the topology displayed by the Bohmian trajectories). One of these contributions is even after interchanging only the modulus or only the phase of the wave packets, while the other one changes its sign after these operations. From the terms that appear in each contribution, it is apparent that the first contribution is associated with the evolution of each separate wave packet as well as with its combination. Thus, it provides information about both the asymptotic behavior of the quantum trajectories and also about the interference process (whenever the condition $\rho_1(x, t)\rho_2(x, t) \approx 0$ is not satisfied). On the other hand, the second contribution describes interference effects connected with the asymmetries or differences of the wave packets. For instance, their contribution is going to vanish if they are identical and coincide on $x = 0$, although their overlapping is nonzero.

With the ingredients given above, let us consider the collision-like case, assuming $\alpha = 1$, both wave packets being identical and propagating in opposite directions at the same speed (see Fig. 2.3). Also, for simplicity in the discussion, we will refer to the regions where ψ_1 and ψ_2 are initially placed as I and II, respectively. In standard quantum mechanics, one is left with the uncertainty of whether ψ_1 , for example, goes to II after interference or, on the contrary, gets back to I (just an analogous situation to a scattering problem of two identical particles). Nonetheless, it is also common to attain a physical reality to the superposition principle, which im-

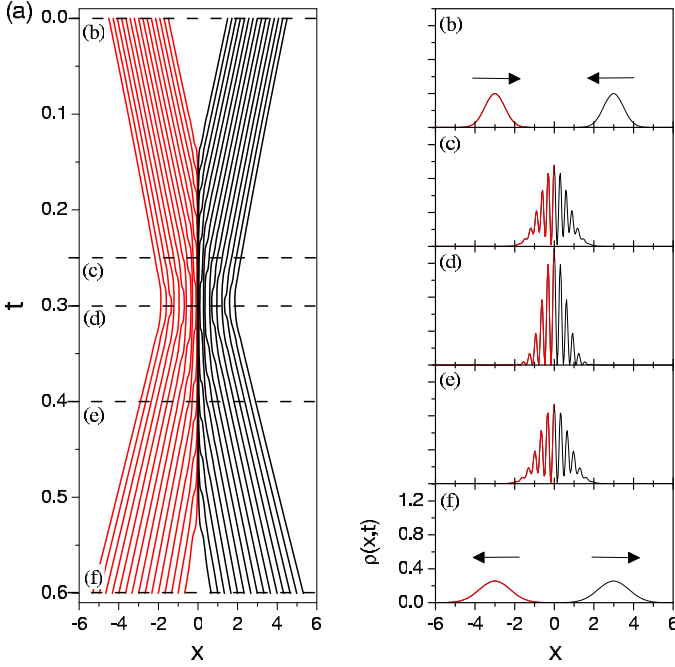


Fig. 2.3 (a) Bohmian trajectories associated with the coherent superposition of two counter-propagating Gaussian wave packets with $v_0 = 10$ and $v_s = 1$. Panels (b)–(f) represent snapshots illustrating the time-evolution of the superposition at the times indicated by the transversal *dashed lines* in panel (a)

plies that, if t_{\max}^{int} denotes the time at which interference is maximum (in this case, this means zero-valued nodes; see Fig. 2.3(d)), then for $t \gg t_{\max}^{\text{int}}$ ψ_1 will continue its evolution in II. Now, the wave packets (or, to be more precise, their probability densities) can be interpreted statistically as describing a swarm of identical, noninteracting quantum particles distributed accordingly. Therefore, combining this fact with the previous view of the superposition principle, one would expect to observe crossings between trajectories for $t \sim t_{\max}^{\text{int}}$. However, as seen in Fig. 2.3, Bohmian trajectories avoid crossing the point $x = 0$ at any time, this leading us to interpret the superposition principle in a different way. We have seen before that quantum dynamics retains information about the system coherence properties through the phase and velocity fields (see Figs. 2.2(b) and (c)). In other words, following (2.8), quantum statistics retains the essence of (quantum) coherence and transmits it to the corresponding quantum dynamics, which translates into a vanishing of the velocity field at $x = 0$ and therefore the impossibility for a net flux of probability (or particles) crossing between regions I and II at any time. Hence trajectories starting in region I, for example, will always keep moving inside this region. Correspondingly, the outgoing wave packet in region I (see Fig. 2.3(f)) accounts for the same swarm of trajectories associated with ψ_1 in Fig. 2.3(b). This whole process can then be un-

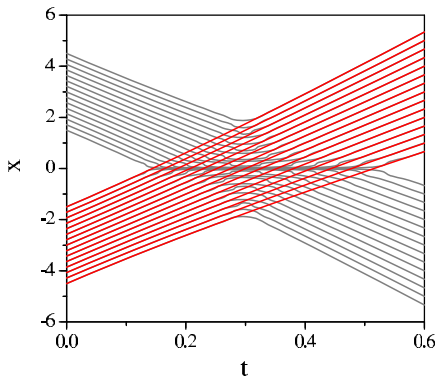


Fig. 2.4 Bohmian trajectories associated with a Gaussian wave-packet superposition (*gray*) and a single Gaussian wave packet (*red*). As it is shown, the presence of two wave packets in a coherent superposition gives rise to a dynamics characterized by trajectories avoiding to cross in the region between the two wave packets. In the asymptotic regime, however, the dynamics is like if the wave packets would have not felt the presence of the other. As in Fig. 2.3, here also $v_0 = 10$ and $v_s = 1$

derstood as a sort of bouncing motion of the wave packets once they have reached the intermediate position between them, as it is highlighted in the panels of the left column of Fig. 2.3 with two different colors.

If the two swarms of trajectories do not cross each other, why then the swarm associated initially with one of the wave packets behaves asymptotically as associated with the other one, as seen in Fig. 2.4? From the conventional picture provided by the superposition principle, the wave packets cross each other. However, from the above Bohmian picture, the process should be understood as a transfer or interchange of probabilities from region I to region II, and vice versa, with the velocity field also changing its sign. Similarly to a particle-particle elastic scattering process, where particles exchange their momenta, here the swarms of particles exchange their probability distributions “elastically”. This is illustrated in Fig. 2.4: after the collision, the two swarms of trajectories (gray lines) bounce backwards and follow the paths that would be pursued by non deflected particles (red lines). A more formal description of this process can be given as follows. Initially, depending on the region where the trajectories are launched from, they are approximately given by

$$\dot{\mathbf{r}}_{\text{I}} \approx \nabla S_1/m \quad \text{or} \quad \dot{\mathbf{r}}_{\text{II}} \approx \nabla S_2/m, \quad (2.9)$$

while asymptotically (i.e., for $t \gg t_{\text{max}}^{\text{int}}$), (2.8) reads as

$$\dot{\mathbf{r}} \approx \frac{1}{m} \frac{\rho_1 \nabla S_1 + \rho_2 \nabla S_2}{\rho_1 + \rho_2}, \quad (2.10)$$

where the approximation $\rho_1(x, t)\rho_2(x, t) \approx 0$ has been used. Now, this approximation also means that the total probability density, $\rho = \rho_1 + \rho_2$, is nonzero only on ρ_1 or ρ_2 . More specifically, in region I, $\rho \approx \rho_2$, while in region II, $\rho \approx \rho_1$. Substituting this result into (2.10) leads to

$$\dot{\mathbf{r}}_{\text{I}} \approx \nabla S_2/m \quad \text{and} \quad \dot{\mathbf{r}}_{\text{II}} \approx \nabla S_1/m, \quad (2.11)$$

which explain the asymptotic dynamics. Thus, although probability distributions transfer, particles remain always within the domains defined by their corresponding initial distributions.

Regarding the diffraction-like case, a similar argumentation can be considered. In this case, spreading is faster than propagation, this giving rise to the well-known Bohmian trajectories typical of two-slit experiments in the *Fraunhofer region* [54, 55]. Here, it is relatively simple to show [56] that the asymptotic solutions of (2.8) read as

$$x(t) \approx 2\pi n \left(\frac{\sigma_0}{x_0} \right) v_s t, \quad (2.12)$$

with $n = 0, \pm 1, \pm 2, \dots$. That is, the initial set of Bohmian trajectories splits up in a series of subsets, each following a *quantized* direction (n) proportional to v_s . Accordingly, if (2.8) is integrated exactly, one will observe quantized bunches of trajectories which, on average, are distributed around the values given by (2.12).

The previous discussion allows us to better understand the implications of the *non-crossing* property of Bohmian mechanics (see Chap. 6, Vol. 1) by making apparent the constraints on the quantum probability flux. This result goes beyond the separability of partial fluxes implicit in the superposition principle and, actually, is in agreement with results obtained with photons [57], where this behavior has been inferred from the experiment. In this regard, it is important to stress that the meaning of *complementarity* should be taken with care. There are no experiments that render *complementary* results depending on whether there is an observer or not; rather, one should talk about two different experiments (see Sect. 2.6.3). This statement appears clearly summarized in Fig. 2.4, again in relation to the superposition principle: interference only appears if the two wave packets are coherently added. For example, in a real two-slit experiment both slits have to be open at the same time, even if mathematically we can compute the solutions (slit diffraction) through each slit separately and add them afterwards. Also, from a practical point of view, phase dynamics are important in order to devise methodologies relying on the concept of Bohmian trajectory [58]: it is not only important to distribute grid points according to ρ , but also having a good sampling of the phase field (or, equivalently, the velocity field), since even for $\rho \approx 0$ the effect of this field can be very important, as seen in Fig. 2.2.

2.3 Interference and Effective Dynamic Potentials

Consider now a Gaussian wave packet scattered off an impenetrable potential wall (for simplicity, we assume $v_0 > v_s$ for now). After some time the wave packet will collide with the wall and then part of it will bounce backwards. The interference of the forward (f) and backward (b) wave packets will lead to a fringe-like pattern similar to those observed in the previous section, with also a time, $t_{\text{max}}^{\text{int}}$, for which the interference fringes are maximally resolved. Putting aside the initial Gaussian shape of the wave packet (and, therefore, the effects associated with v_s), if this process is

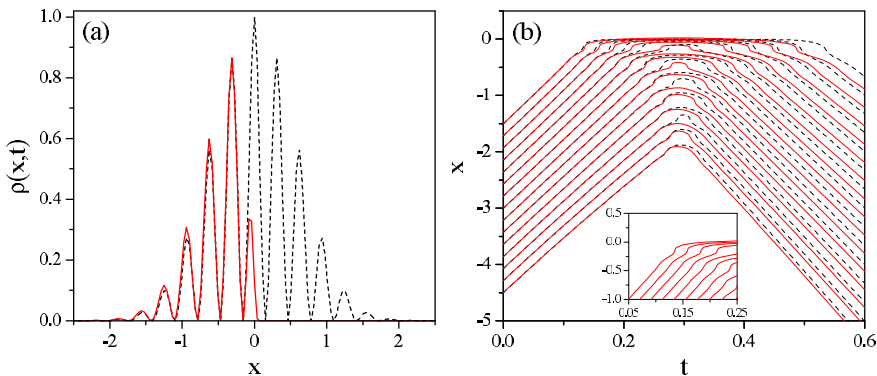


Fig. 2.5 (a) Probability density at $t = 0.3$ for the collision of a Gaussian wave packet off: the external potential described by (2.16) (red-solid line) and another (identical) Gaussian wave packet (black-dashed line). To compare with, the maxima at $x \approx -0.32$ of both probability densities are normalized to the same height (the maximum at $x = 0$ of the two wave packet probability density being set to unity). (b) Bohmian trajectories illustrating the dynamics associated with the two cases displayed in part (a). *Inset*: enlargement of the plot around $t = 0.15$ to show the action of the potential well on the trajectories started closer to $x = 0$. Here, $v_0 = 10$ and $v_s = 1$

represented as

$$\Psi = \psi_f + \psi_b \sim e^{imv_0x/\hbar} + e^{-imv_0x/\hbar} \quad (2.13)$$

at t_{\max}^{int} , we obtain $\rho(x) \sim \cos^2(mv_0x/\hbar)$. The distance between two consecutive minima is then $w_0 = \pi\hbar/mv_0$, which turns out to be the same distance between two consecutive minima in the two wave-packet interference process. That is, although each process has a different physical origin (barrier scattering vs wave packet collision), the effect is similar—there is a certain shift in the position of the corresponding maxima ($\sim\pi/2$), which arises from the fact that, in the case of barrier scattering, the impenetrable wall forces the wave function to have a node at $x = 0$. If now we go to the corresponding quantum trajectories, we observe in Fig. 2.5 that as the wave packet starts to “feel” the presence of the wall, the trajectories bend gradually (in the x vs t representation) and then start to move in the opposite direction. When these trajectories are compared with those associated with the problem of the two wave-packet superposition, the resemblance between trajectories with the same initial positions is excellent, except in the interference region due to the different location of the nodes of the corresponding wave functions—these differences are the trajectory counterpart of the shift mentioned before.

From the previous description one might infer that, since the dynamics for $x < 0$ and for $x > 0$ do not mix (due to non-crossing), each half of the central interference maximum arises from different groups of trajectories. Thus, in principle, one should be able to arrange the impenetrable wall problem in such a way that allows us to explain this effect. Within this context, although all the peaks have the same width as in the wave-packet superposition problem, the closest one to the wall should have half such a width, i.e., $w \sim \pi\hbar/2p_0 = w_0/2$. Due to boundary conditions and the

forward-backward interference discussed above, it is clear that this peak cannot arise from interference, but from another mechanism: a *resonance* process. Therefore, apart from the wall, we also need to consider the presence of a potential well. In order to observe a resonance or quasi-bound state, the width of this well should be, at least, of the order of the width w of the bound state. From standard quantum mechanics, we know that in problems related to bound states in finite well potentials the relationship [59]

$$V_0 a^2 = n \frac{\hbar^2}{2m} \quad (2.14)$$

always appears, where a is the half-width of the well ($a = w/2$) and n is an integer number. The eventual solutions (bound states) are then observable or not depending on whether the condition which it might correspond will be in consonance or not with this condition. In our case, we can use (2.14) to obtain an estimate of the well depth, which results

$$V_0 = \frac{16}{\pi^2} \frac{p_0^2}{2m}, \quad (2.15)$$

when we assume $n = 1$. Now, we have then a potential which presents a short-range attractive well before reaching the impenetrable wall,

$$V(x) = \begin{cases} 0 & x < -w \\ -V_0 & -w \leq x \leq 0 \\ \infty & 0 < x. \end{cases} \quad (2.16)$$

If we compute now $\rho(\mathbf{r}, t)$ at t_{\max}^{int} , we obtain the result displayed in Fig. 2.5(a). As can be noted, now there is an excellent matching of the peak widths, with the closest one to the wall being half-width when compared with the remaining ones—the associate quantum trajectories are displayed and compared in Fig. 2.5(b).

The equivalence between the two wave packet collisions and the scattering of a wave packet off a potential does not restrict to the condition $v_0 > v_s$, but is of general validity. As shown in Fig. 2.6, it also holds for the diffraction-like situation, i.e., $v_0 < v_s$. In Fig. 2.6(a), we show the corresponding diffraction-like pattern is again well reproduced after replacing one of the wave packets by an external potential, and the same also happens for the corresponding quantum trajectories (see Fig. 2.6(b)). However, in order to find these results, now a subtlety has to be considered: the central diffraction maximum increases its width with time. In terms of simulating this effect with a potential function, it is clear that the width of the potential well should also increase with time. Thus, we need to consider a “dynamical” or time-dependent potential function rather than a static one, as done before. In order to determine this potential function, we proceed as before. First, we note that the two

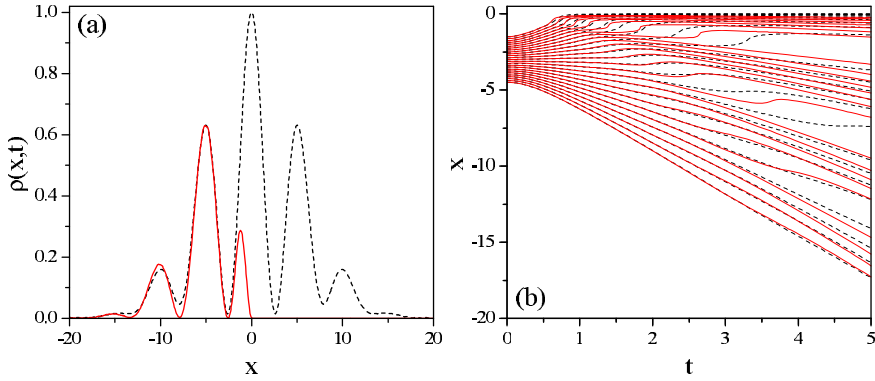


Fig. 2.6 (a) Probability density at $t = 5$ for the collision of a Gaussian wave packet off: the external, time-dependent potential described by (2.26) (red-solid line) and another (identical) Gaussian wave packet (black-dashed line). To compare with, the maxima at $x \approx -5$ of both probability densities are normalized to the same height (the maximum at $x = 0$ of the two wave packet probability density being set to unity). (b) Bohmian trajectories illustrating the dynamics associated with the two cases displayed in part (a). Here, $v_0 = 0.1$ and $v_s = 1$

wave-packet collision problem, (2.3), is explicitly written in terms of Gaussian wave packets (see (5.1)) as

$$\begin{aligned} \Psi \sim & e^{-(x+x_t)^2/4\tilde{\sigma}_t\sigma_0 + ip_0(x+x_t)/\hbar + iE_0t/\hbar} \\ & + e^{-(x-x_t)^2/4\tilde{\sigma}_t\sigma_0 - ip_0(x-x_t)/\hbar + iE_0t/\hbar}, \end{aligned} \quad (2.17)$$

where

$$x_t = x_0 - v_0 t \quad (2.18)$$

(for simplicity, we have neglected the time-dependent normalization prefactor, since it is not going to play any important role regarding either the probability density or the quantum trajectories). The probability density associated with (2.17) is

$$\rho(x, t) \sim e^{-(x+x_t^2)/2\sigma_t^2} + e^{-(x-x_t^2)/2\sigma_t^2} + 2e^{-(x^2+x_t^2)/2\sigma_t^2} \cos[f(t)x], \quad (2.19)$$

with

$$f(t) \equiv \frac{2p_0}{\hbar} + \frac{\hbar t}{2m\sigma_0^2} \frac{x_t}{\sigma_t^2}. \quad (2.20)$$

As can be noted, (2.19) is maximum when the cosine is $+1$ (constructive interference) and minimum when it is -1 (destructive interference). The first minimum (with respect to $x = 0$) is then reached when $f(t)x = \pi$, i.e.,

$$x_{\min}(t) = \frac{\pi}{\frac{2p_0}{\hbar} + \frac{\hbar t}{2m\sigma_0^2} \frac{x_t}{\sigma_t^2}} = \frac{\pi\sigma_t^2}{\frac{2p_0\sigma_0^2}{\hbar} + \frac{\hbar t}{2m\sigma_0^2} x_0}, \quad (2.21)$$

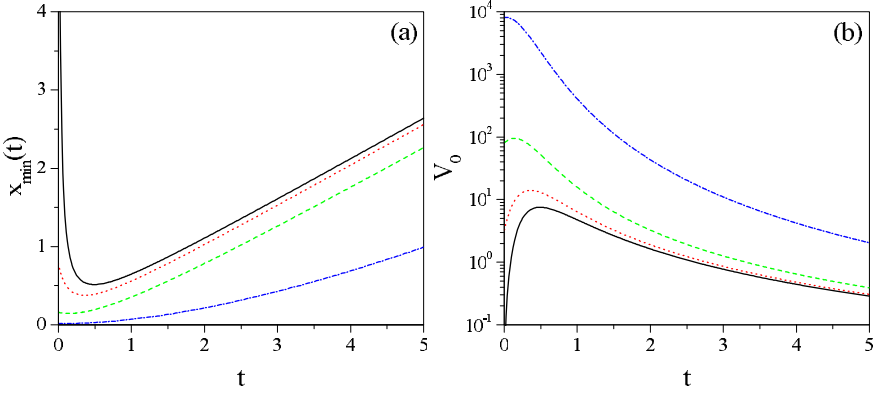


Fig. 2.7 (a) Plot of x_{\min} as a function of time for different values of the propagation velocity: $v_0 = 0.1$ (black solid line), $v_0 = 2$ (red dotted line), $v_0 = 10$ (green dashed line) and $v_0 = 100$ (blue dash-dotted line). (b) Plot of V_0 as a function of time for the same four values of v_0 considered in panel (a). In all cases, $v_s = 1$

for which

$$\rho[x_{\min}(t)] \sim 4e^{-(x_{\min}^2 + x_t^2)/2\sigma_t^2} \sinh\left(\frac{x_{\min}x_t}{2\sigma_t^2}\right), \quad (2.22)$$

which basically is zero if the initial distance between the two wave packets is relatively large when compared with their spreading.

In Fig. 2.7(a), we can see the function $x_{\min}(t)$ for different values of the propagation velocity v_0 . As seen, $x_{\min}(t)$ decreases with time up to a certain value, and then increases again, reaching a linear asymptotic behavior. From (2.21) we find that the minimum value of $x_{\min}(t)$ is reached at

$$t_{\min} = \frac{4m\sigma_0^4}{\hbar^2 x_0} \left[-p_0 + \sqrt{p_0^2 + p_s^2 \left(\frac{x_0}{\sigma_0} \right)^2} \right]. \quad (2.23)$$

The linear time-dependence at long times is characteristic of the Fraunhofer regime, where the width of the interference peaks increases linearly with time. On the other hand, the fact that, at $t = 0$, $x_{\min}(t)$ increases as v_0 decreases (with respect to v_s) could be understood as a “measure” of the coherence between the two wave packets, i.e., how important the interference among them is when they are far apart (remember that, despite their initial distance, there is always an oscillating term in between due to their coherence [60]). Note that this is in accordance with the standard quantum-mechanical arguments that interference-like patterns are manifestations of the wavy nature of particles, while scattering-like ones display their corpuscle nature (more classical-like). Thus, as the particle becomes more “quantum-mechanically”, the initial reaching of the “effective” potential well should be larger. And, as the particle behaves in a more classical fashion, this reaching should decrease and be only relevant near the scattering or interaction region, around $x = 0$. From (2.21),

two limits are thus worth discussing. In the limit $p_0 \sim 0$,

$$x_{\min}(t) \approx \frac{\pi \sigma_t^2}{x_0} \frac{\tau}{t} \quad (2.24)$$

and $t_{\min} \approx \tau$. In the long-time limit, this expression becomes $x_{\min}(t) \approx (\pi \hbar / 2m)(t/x_0)$, i.e., x_{\min} increases linearly with time, as mentioned above. On the other hand, in the limit of large σ_0 (or, equivalently, $v_0 \gg v_s$),

$$x_{\min}(t) \approx \frac{\pi \hbar}{2p_0} \quad (2.25)$$

and $t_{\min} \approx 0$. That is, the width of the “effective” potential barrier remains constant in time, this justifying our former hypothesis above, in the scattering-like process, when we considered $w \sim \pi \hbar / 2p_0$.

After (2.21), the time-dependent “effective” potential barrier is defined as (2.16),

$$V(t) = \begin{cases} 0 & x < x_{\min}(t) \\ -V_0[x_{\min}(t)] & x_{\min}(t) \leq x \leq 0 \\ \infty & 0 < x \end{cases} \quad (2.26)$$

with the (time-dependent) well depth being

$$V_0[x_{\min}(t)] = \frac{2\hbar^2}{m} \frac{1}{x_{\min}^2(t)}. \quad (2.27)$$

The variation of the well depth along time is plotted in Fig. 2.7(a) for the different values of v_0 considered in Fig. 2.7(b). As seen, the well depth increases with v_0 (in the same way that its width, x_{\min} , decreases with it) and decreases with time. For low values of v_0 , there is a maximum, which indicates the formation of the quasi-bound state that will give rise to the innermost interference peak (with half the width of the remaining peaks, as shown in Fig. 2.6(a)). Note that, despite the time-dependence of the well depth, in the limit $v_0 \gg v_s$, we recover (2.15).

We have shown that the problem of the interference of two colliding wave packets can be substituted by the problem of the collision of a wave packet off a potential barrier. Although the model that we have presented is very simple, it is important to stress that it reproduces fairly well the dynamics involved—of course, one can always search for more refined and precise models. The fact that one can make this kind of substitutions puts quantum mechanics and the superposition principle on the same grounds as two important frameworks in classical physics (one could think of many other situations, but these two ones are particularly general and well known). The first one is widely used in classical mechanics (and then, in its quantized version, also in quantum mechanics): it is the equivalence between a two-body problem and a one-body problem acted by a central force. As expected, our reduction is of the same kind: a two wave-packet dynamical process can be reduced to the dynamics of a single wave packet subjected to the action of an external potential. The second framework is the one provided by the so-called method of images, widely used in

electrostatics: the interaction between a charge distribution and a conductor can be replaced by the interaction between such a charge distribution and another virtual one. This would be the reciprocal situation to ours: the dynamics induced by an external potential on a wave packet can be translated as the dynamics taking place when two wave packets (ours and a virtual one) are present.

2.4 Analogy Between Collisions and Wave-Packet Interference

In the previous section we have studied interference processes with identical Gaussian wave packets propagating symmetrically with respect to $x = 0$. However, what happens in other more general situations where neither the wave packets are identical nor their weights? Although one could think of many different possibilities, it is enough to consider three cases in order to already obtain an insight on the related physics. The criterion followed to classify these cases is based on which property of the wave packets is varied (with respect to the symmetric case described above) or considered at a time:

1. Different modulus of the initial average momentum ($|p_{01}| \neq |p_{02}|$).
2. Different initial spreading ($\sigma_{01} \neq \sigma_{02}$).
3. Different weights ($c_1 \neq c_2$ or, equivalently, $\alpha \neq 1$).

Since the collision-like case is simpler to understand than the diffraction-like one, below we will assume $v_0 \gg v_s$, although generalizing to any v_0/v_s ratio is straightforward. Moreover, as before, the initial distance between both wave packets is such that the initial overlapping is negligible.

Case (1) is represented in Fig. 2.8, where we can observe that varying the moduli of the initial average momenta only produces an asymmetric shift of the final positions of the wave packets with respect to $x = 0$ (see panel (a)), which is a result of the distortion of the boundary between regions I and II (the final wave packets are not symmetrically distributed with respect to $x = 0$). This boundary evolves in time at the same constant velocity than the corresponding expected value of the velocity for the total superposition,

$$\bar{v}_A = \frac{\bar{p}_A}{m} = \frac{\langle \Psi_A^* | \hat{p} | \Psi_A \rangle}{m} = \frac{p_{01} + p_{02}}{2m}, \quad (2.28)$$

because both wave packets are identical and normalized (see (5.1)). In particular, since $p_{01} = 10$ and $p_{02} = -30$, we have $\bar{v}_A = -10$. Integrating the equation of motion $\dot{\bar{x}}_A = \bar{v}_A$ (according to Ehrenfest's theorem [59]), we obtain

$$\bar{x}_A(t) = \bar{x}_0 + \bar{v}_A t, \quad (2.29)$$

with $\bar{x}_0 = \langle \Psi^* | \hat{x} | \Psi \rangle = (x_{01} + x_{02})/2$. Equation (2.29) describes the time-evolution of the boundary between regions I and II in this case—note that for $p_{02} = -p_{01}$, we recover again the time-independent boundary found for identical wave packets,

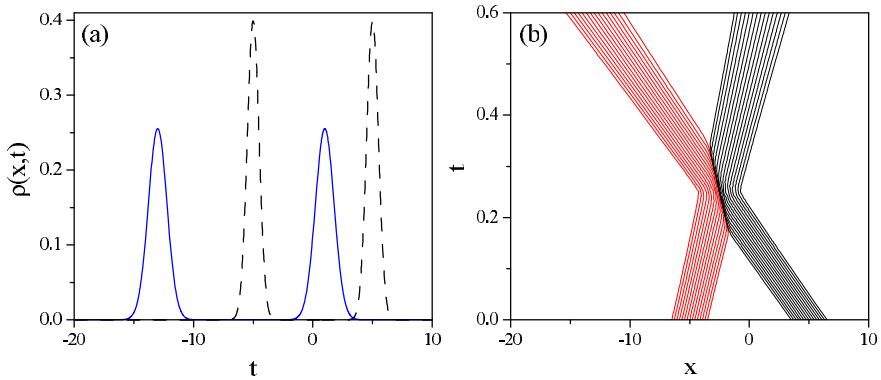


Fig. 2.8 (a) Probability density at $t = 0$ (black-dashed line) and $t = 0.6$ (blue-solid line) for a wave packet superposition with $p_{01} = 10$ and $p_{02} = -30$. The value of the other relevant parameters are $\sigma_{01} = \sigma_{02} = 0.5$ and $\alpha = 1$. (b) Quantum trajectories associated with the dynamics described by the situation displayed in panel (a)

studied in the previous section. As expected, this boundary also defines the non-crossing line for the associate quantum trajectories, which forbids the trajectory transfer from one region to the other one and vice versa, as seen in Fig. 2.8(b). Because of this property, we find that the two wave packets behave like two classical particles undergoing an elastic scattering: there is only transfer (indeed, exchange) of momentum during the scattering process, but the net balance of probability is zero since no trajectories are transferred. Moreover, note that indeed this effect will not be noticeable unless one looks at the quantum trajectories—as seen in panel (a), the evolution of the wave packets does not provide any clue on it.

In case (2), since both velocities are equal in modulus, after interference the centers of the outgoing wave packets occupy symmetric positions with respect to $x = 0$, as seen in Fig. 2.9(a) (only the different width disturbs the full symmetry). However, as in case (1), the lack of total symmetry also causes the distortion of the boundary between regions I and II (see panel (b)), with a similar behavior regarding the non-crossing (or non-transfer) property. Now, since the modulus of both momenta are the same, $\langle \Psi^* | \hat{p} | \Psi \rangle = 0$ and therefore we cannot appeal to the same argument as before to explain this distortion effect. However, there is still a sort of effective “internal” momentum which depends on the ration between the widths of the wave packets. Assuming that the spreading is basically constant for the time we have propagated the trajectories, the corresponding effective velocity is given by

$$\bar{v}_B = \frac{\sigma_{01}^{-1} v_{01} + \sigma_{02}^{-1} v_{02}}{\sigma_{01}^{-1} + \sigma_{02}^{-1}} = \left(\frac{\sigma_{02} - \sigma_{01}}{\sigma_{01} + \sigma_{02}} \right) v_0, \quad (2.30)$$

with $v_{01} = v_0 = -v_{02}$ ($v_0 > 0$); since the width of the wave packets varies in time, a slight time-dependence can be expected in \bar{v}_B , although in our case, as can be noticed from Fig. 2.9(b), it can be neglected for practical purposes. Substituting the

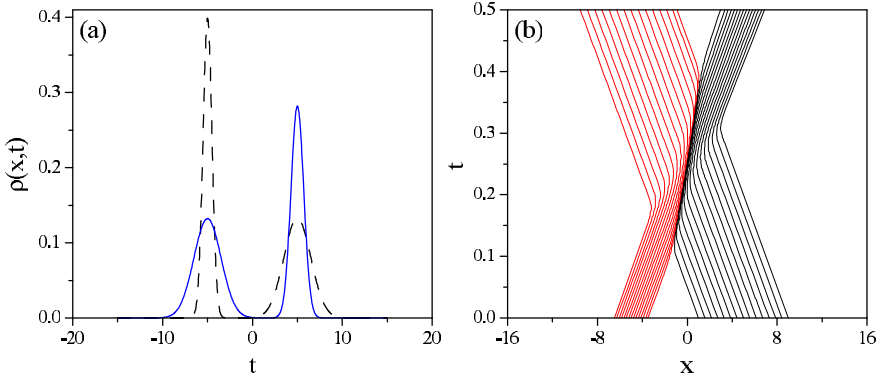


Fig. 2.9 (a) Probability density at $t = 0$ (black-dashed line) and $t = 0.8$ (blue-solid line) for a wave packet superposition with $\sigma_{01} = 0.5$ and $\sigma_{02} = 1.5$. The value of the other relevant parameters are $|p_{01}| = |p_{02}| = 20$ and $\alpha = 1$. (b) Quantum trajectories associated with the dynamics described by the situation displayed in panel (a)

numerical values used in the propagation into (2.30), we find $\bar{v}_B = 5$. The boundary or non-crossing line will be then given by

$$\bar{x}_B(t) = \bar{x}_0 + \bar{v}_B t, \quad (2.31)$$

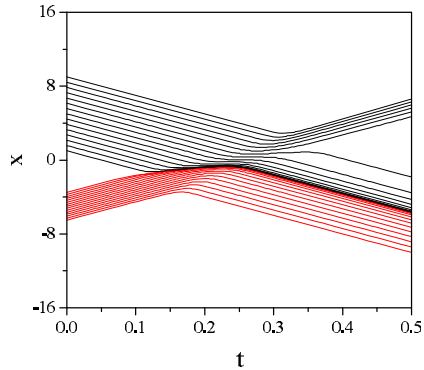
where

$$\bar{x}_0 = \frac{\sigma_{01}^{-1} x_{01} + \sigma_{02}^{-1} x_{02}}{\sigma_{01}^{-1} + \sigma_{02}^{-1}} = -\left(\frac{\sigma_{02} - \sigma_{01}}{\sigma_{01} + \sigma_{02}} \right) x_0, \quad (2.32)$$

with $x_{02} = -x_{01} = x_0$ ($x_0 > 0$)—note that, otherwise, $\bar{x}_0 = 0$, as infers from Fig. 2.9(a), since the larger width of one of the wave packets balances the effect of the larger height of the other one. Despite this internal redistribution or balance of momentum, it is clear that we find again, as in case (1), an elastic collision-like behavior.

The effect of an effective internal momentum could be explained by considering that, in this case, the relative size of the wave packets acts like a sort of *quantum inertia* or effective mass. Consider the trajectories associated with the wave packet with smaller value of σ_0 (black trajectories in Fig. 2.9(b)). As can be seen, it takes approximately 0.2 time units the whole swarm to leave the scattering or collision region (along the non-crossing boundary)—or, equivalently, to revert the sign of the momentum of all the trajectories constituting the swarm and get their final asymptotic momenta. On the other hand, the trajectories associated with the wave packet with larger σ_0 (red trajectories in Fig. 2.9(b)) revert their momenta much faster, in about 0.1 time units—of course, we are not considering here the time that trajectories remain moving along the boundary, since the total “interaction” time has to be the same for both swarms of trajectories. Thus, we find that the larger the spreading momentum, the larger also the quantum inertia of the swarm of particles to change the propagation momentum and, therefore, to reach the final state.

Fig. 2.10 Bohmian trajectories associated with a Gaussian wave-packet superposition with $\sigma_{01} = 0.5$ and $\sigma_{02} = 1.5$. The value of the other relevant parameters are $p_{01} = -p_{02} = 20$ and $\alpha = 1$



We would also like to note another interesting property associated with case (2). Consider that both wave packets lack their corresponding normalizing factor A_t when introduced in the superposition. If we then compute the expected value of the momentum, for instance, we obtain

$$\langle \hat{p} \rangle_B = \frac{\langle \Psi_B^* | \hat{p} | \Psi_B \rangle}{\langle \Psi_B^* | \Psi_B \rangle} = \frac{\sigma_{01} v_{01} + \sigma_{02} v_{02}}{\sigma_{01} + \sigma_{02}} = \left(\frac{\sigma_{01} - \sigma_{02}}{\sigma_{01} + \sigma_{02}} \right) p_0, \quad (2.33)$$

i.e., there should be a certain “drift” towards region I, such as in case (2)—and the same holds if we compute instead the expected value of the position. Note that in the previous case the normalization of each Gaussian wave packet produces a balance: the probability with which each wave packet contributes to the superposition is the same ($c_1^2 = c_2^2 = 1/2$) because the width of one compensates the height of the other, as explained above. Therefore, the expected value of both position and momentum have to be zero. However, this compensation does not happen now: both wave packets have the same height although their widths differ, thus contributing with different probabilities P to the superposition,

$$P_1 = \frac{\sigma_{01}}{\sigma_{01} + \sigma_{02}} \quad \text{and} \quad P_2 = \frac{\sigma_{02}}{\sigma_{01} + \sigma_{02}}, \quad (2.34)$$

which produce the results observed in Fig. 2.10 (again, we assume that $\sigma_t \approx \sigma_0$ for the time considered). However, by inspecting (2.33), we note that if we add the averaged momentum $\bar{p}_B = m \bar{v}_B$, the total average momentum vanishes. Somehow the averaging defined by (2.33) acts as in classical mechanics, when a certain magnitude (e.g., the position or the momentum) is computed with respect to the center of mass of a system. Here, \bar{p}_B is the magnitude necessary to reset the superposition of non normalized Gaussian wave packets to a certain “center of spreading”. On the other hand, it is also important to stress the fact that, in this case, the clear boundary between the swarms of trajectories associated with each initial wave packet disappears. Now, although there is still a boundary, it does not prevent for the transfer of trajectories from one region to the other, as before. This effect, similar to consider inelastic scattering in classical mechanics, arises as a consequence of having wave packets with different probabilities.

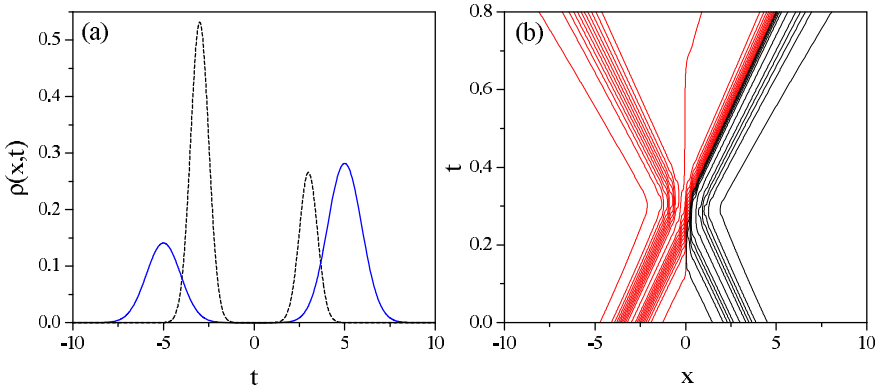


Fig. 2.11 (a) Probability density at $t = 0$ (black-dashed line) and $t = 0.8$ (red-solid line) for a wave packet superposition with $\alpha = 0.5$ (i.e., $c_1^2 = 2/3$ and $c_2^2 = 1/3$). The value of the other relevant parameters are $p_{01} = -p_{02} = 10$ and $\sigma_{01} = \sigma_{02} = 0.5$. (b) Quantum trajectories associated with the dynamics described by the situation displayed in panel (a). The initial conditions for the quantum trajectories have been assigned by considering the different weights associated with each wave packet

As seen above, unless there is an asymmetry in the probabilities carried by each partial wave in the superposition, there is always a well-defined boundary or non-crossing line between regions I and II. However, in the second example of case (2), we have observed that it is enough an asymmetry in the probability distribution to break immediately the non-crossing line. Instead of using non normalized Gaussian wave packets, let us consider case (3), which is equivalent although the asymmetry is caused by $\alpha \neq 1$ instead of the wave-packet normalization. As we have seen in the two previous cases, provided both wave packets have the same weight (or, at least, both contribute equally to the superposition), the corresponding quantum trajectories, even if they are evenly distributed (equidistant) along a certain distance initially, they are going to give a good account of the whole dynamics. However, if the weights change, the same does not hold anymore. Somehow equal weights (or equal probabilities) means the division of the coordinate space into two identical regions, each one influenced only by the corresponding wave packet. In other words, there are always two well-defined swarms of trajectories, each one associated with one of the initial wave packets. When the weights change, apparently we have something similar to what we have been observing until now: the wave packets exchange their positions (see Fig. 2.11(a)). However, when we look at the associated quantum trajectories, we realize that there is transfer or flow of trajectories from one of the initial swarms to the other one. This transfer takes place from the swarm with larger weight to the lesser one, thus distorting importantly the boundary between regions I and II, as seen in Fig. 2.11(b), where this boundary lies somewhere between the two trajectories represented in blue (the trajectories that are closer to $x = 0$ in each swarm). However, note that this does not imply that the number of trajectories varies in each region asymptotically, but only the number of

them belonging to one or the other wave packet. Thus, if initially we have $N_1 \propto c_1^2$ trajectories associated with ψ_1 and $N_2 \propto c_2^2$ with ψ_2 , asymptotically we will observe $N'_1 = (1 - \alpha)N_1 \propto c_2^2$ and $N'_2 = N_2 + \alpha N_1 \propto c_1^2$ due to the trajectory transfer. Unlike the two previous cases discussed above, this process can be then compared with inelastic scattering, where, after collision, not only the probability fluxes but also the number of particles changes. Accordingly, it is also important to mention that, due to the trajectory transfer, representations with evenly distributed trajectories are not going to provide a good picture of the problem dynamics, as infers from Fig. 2.10. Rather, we can proceed in two different ways. The obvious procedure is to consider initial positions distributed according to the corresponding (initial) probability densities. This procedure carries a difficulty: the number of trajectories needed to have a good representation of the dynamics may increase enormously depending on the relative weights. The second procedure is to consider evenly spaced values of the probability density and allocate at such space points the initial positions of the trajectories, as we have done to construct Fig. 2.11(b). In this case, although the trajectories will not accumulate exactly along the regions with larger values of the probability density, this construction has the advantage that we can follow the transport of equi-spaced probabilities along each particular trajectory. To make more apparent the difference in the relative number of trajectories (probability density) associated with each initial wave packets, we have considered $N_1 = 23$ and $N_2 = 11$ (i.e., $N_2/N_1 \sim 0.48 \approx c_2^2/c_1^2 = 0.5$). After scattering, the numbers that we have are $N'_1 = 11$ and $N'_2 = 23$, which are in the expected ratio $c_2'^2/c_1'^2 = c_1^2/c_2^2 = 2$.

As said at the beginning of this section, here we have only taken into account the collision-like case. The same kind of results are expected for the analogous diffraction-like cases, with the addition that they manifest as a loss of fringe visibility. Thus, for cases A and B, one could appreciate a well define non-crossing line and a loss of fringe visibility due to the divergent velocities, v_0 and v_s , respectively. And, for case C (or the second example in case B), the loss of fringe visibility would be caused by the transfer of trajectories, which would also lead to the distortion of the non-crossing line.

2.5 Interference in a Complex Configuration Space

Interference phenomena in a complex configuration space display a rich dynamical effects, such as the formation of *quantum caves* [61, 62]. In order to understand the appearance of these effects, consider the analytical continuation of the superposition (2.3) to the complex plane. Within a real quantum Hamilton-Jacobi (RQHJ) formulation (the standard Bohmian mechanics) at least two dimensions are necessary in order to observe quantum vorticity [63, 64]. However, as shown below, only one dimension is required to observe the same phenomenon within the CQHJ framework provided quantum interference is involved. The collision of two identical Gaussian wave packets in one dimension constitutes an ideal scenario which illustrates fairly well the appearance of vorticity in the complex plane. Before entering into details,

first we would like to specify that by collision of two wave packets (either Gaussian or of any other general type) here we mean the problem described by a “one-body” wave function which consists of a wave packet superposition. These wave packets fulfill two conditions initially: (a) they move towards each other and (b) their respective propagation velocities are larger than their spreading rates. With these conditions, after the collision (maximal interference) takes place, two emerging or outgoing wave packets are clearly defined, just like in a classical elastic particle-particle scattering problem. Interference-like situations, i.e., those where typical interference pattern can be observed after the collision instead of two emerging wave packets, constitute the opposite case.

In the complex version of the wave packet interference process, the dynamics becomes richer: this one-dimensional problem unfolds into a two-dimensional one on the complex or *Argand* plane, with the dynamics exhibiting more intricate features. Here, we are dealing with complex fields (the wave function and the velocity) which are functions of a complex variable and time. In order to provide a clear picture of the time-evolution of these fields, we will decompose both of them in polar form, i.e.,

$$\mathcal{F}(z, t) = \varrho_{\mathcal{F}}(z, t) e^{i\varphi_{\mathcal{F}}(z, t)}, \quad (2.35)$$

where $\varrho_{\mathcal{F}}(z, t)$ and $\varphi_{\mathcal{F}}(z, t)$ represent, respectively, the modulus and the phase of the complex field $\mathcal{F}(z, t)$ —in our case, \mathcal{F} stands for $\tilde{\Psi}$ and \tilde{v} . Thus, in Fig. 2.12 the contour plots of $\varrho_{\tilde{\Psi}}$, $\varrho_{\tilde{v}}$ and $\varphi_{\tilde{v}}$ are displayed at four different times to illustrate the dynamical evolution in the complex plane. We have not plotted the field $\varphi_{\tilde{\Psi}}$ because it is highly oscillating in the space (i.e., on the Argand plane) and time ranges considered, and therefore, very difficult to visualize; instead, we have shown the fields $\varrho_{\tilde{v}}$ and $\varphi_{\tilde{v}}$, which are related and provide a more clear information. Several remarks are worth stressing. First, as can be inferred from the sequence presented in the upper row of Fig. 2.12, $\Psi(x, t)$ corresponds to the value of $\tilde{\Psi}(z, t)$ along the real axis ($z_r = x$, $z_i = 0$) at the time t . Second, $\tilde{\Psi}$ satisfies the normalization condition *only* along the real axis, but not in general on the complex plane. And, third, following the sequence in Fig. 2.12 (from left to right), we observe that the interference process translates into a two-dimensional anticlockwise rotating dynamics, where at t_{\max} the nodal structure—a set of aligned nodes—just lies on the real axis. At any other time, there is still a nodal alignment, but it is out of the real axis. This explains why, in real space, interference is weaker at any other time than t_{\max} (in other words, the larger $|t - t_{\max}|$, the weaker the interference pattern). Conversely, as \tilde{v} shows, the nodal structure remains even for relatively large times ($t \gg t_{\max}$) in the complex space. Taking into account all these observations, we can say that, within this (complex) formulation, the evolution of (real) Ψ can be understood as an “apparent” effect of the evolution of $\tilde{\Psi}$ in the complex plane. That is, the value displayed by Ψ at each time can be compared with the frames of a movie tape (which is the role played by $\tilde{\Psi}$); each frame is watched only when the corresponding piece of the tape is passing in front of the projector. The sensation of motion then appears when the tape runs in front of the projector (i.e., many frames passing consecutively).

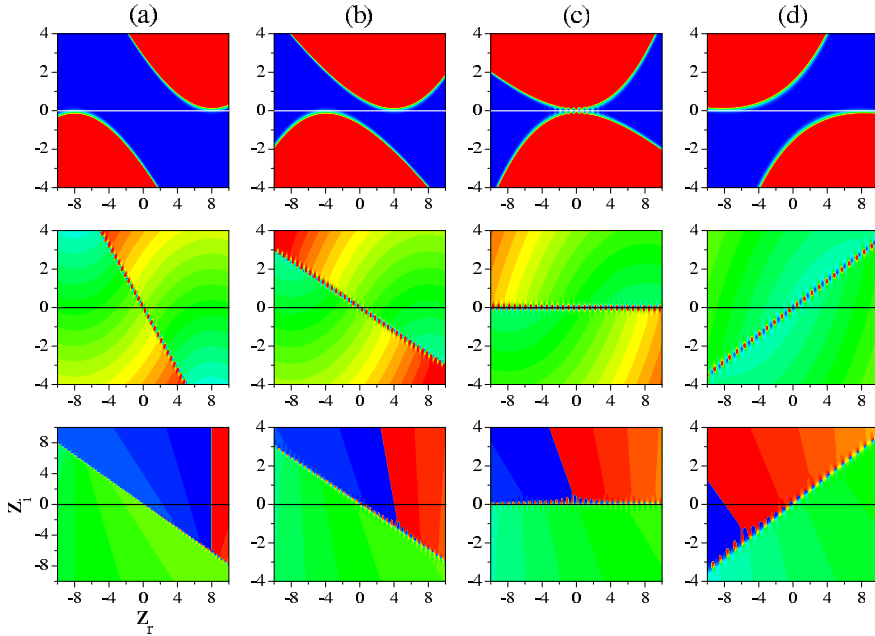


Fig. 2.12 The *three* rows, from top to bottom, correspond to the contour plots of $Q_{\bar{\psi}}$, $Q_{\bar{v}}$ and $\varphi_{\bar{v}}$, respectively, at: (a) $t = 0$, (b) $t = 2$, (c) $t = 4$, and (d) $t = 8$ (arbitrary units are used). The color scale from red to blue ranges from high values of the corresponding field to low ones (0 in the *top* and *middle* rows, and negative in the *bottom* one). The real axis is denoted by the white/black solid line at $z_i = 0$. The parameters considered in the simulations are the same as those used in Fig. 2.2

In Fig. 2.13, the evolution from $t = 0$ to $t = 8$ for four different families of complex trajectories is plotted. Each family represents a set of *isochrones* (see Chap. 6 in Vol. 1) [65–70], i.e., all the trajectories belonging to the same family cross the real axis (their imaginary part, z_i , vanishes) at a given time, namely the crossing time t_c (in the cases depicted, at $t_c = 0, 2, 4$ and 8 , respectively). Moreover, in our case, the trajectories of each family have been chosen in such a way that their respective real part coincide with the positions of the real trajectories in Fig. 2.2 at the time they cross the real axis. Comparing the real and complex trajectory dynamics, it is clear that there is no a simple one-to-one correspondence between both types of trajectories, although they are associated with the same physical problem; real trajectories are not the real part of the complex ones at any time, as suggested elsewhere [71–73]. To establish a connection, one has to consider the movie-based analogy between Ψ and $\bar{\Psi}$ pointed out above and the previous discussion in terms of isochrones. Accordingly, a single real trajectory is made of the crossings of many *different* complex trajectories with the real axis—one crossing for each (real) position at each time. Note that this allows us to define a real trajectory as a family of complex trajectories fulfilling the property that their subsequent crossings (in time) with the real axis generate such a real trajectory. This is, precisely, the reason

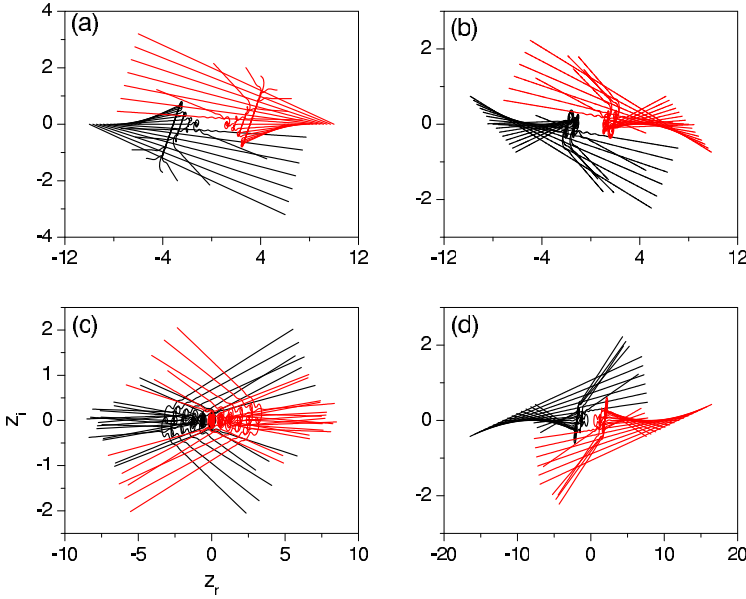


Fig. 2.13 Isochrones crossing the real axis [$z_i(t_c) = 0$] at: (a) $t_c = 0$, (b) $t_c = 2$, (c) $t_c = 4$, and (d) $t_c = 8$, in accordance with the snapshots shown in Fig. 2.12 (arbitrary units are used). All the trajectories are propagated from $t = 0$ up to $t = 8$; the crossing points correspond to the same positions reached by the real trajectories in Fig. 2.2 at the corresponding times. *Black and red trajectories* are associated with ψ_1 and ψ_2 , respectively

why when using computational methods based on complex trajectories one needs to consider isochrones to reproduce the corresponding observable [65–70]. As seen in Fig. 2.13(c), some of these isochrones can display the effects of a vortical dynamics, unlike the analogous situation in real configuration space, where vorticity can only be observed in two (or higher) dimensions [63, 64]—nevertheless, the presence of vortices in complex space can be explained as in a real dynamical framework (see below). The appearance of this dynamics breaks off the causticity regime associated with free wave packet propagation, where (complex) quantum trajectories give rise to the appearance of *caustics*, i.e., curves arising as the envelope of a set of trajectories (all of them tangent to such a curve at different, consecutive times). This can be seen in panels (a), (b) and (d) of Fig. 2.13. Before and after t_{\max} , the nearly free propagation of ψ_1 and ψ_2 manifests as a sort of causticity regime, which can not be appreciated at all under a strong vortical dynamics, as seen in Fig. 2.13(c), where this dynamics prevents the isochrones to display the corresponding caustics.

The equation of motion for complex quantum trajectories arises after substituting the complex-valued wave function in polar form, $\Psi(x, t) = \exp[iS(x, t)/\hbar]$, into the time-dependent Schrödinger equation. This yields the complex-valued quantum Hamilton-Jacobi equation

$$-\frac{\partial S}{\partial t} = \frac{1}{2m} \left(\frac{\partial S}{\partial x} \right)^2 + V(x) + \frac{\hbar}{2mi} \frac{\partial^2 S}{\partial x^2}, \quad (2.36)$$

where $S(x, t)$ is the complex action and the last term is the complex quantum potential, $Q(x, t)$. For the system studied here, no external interaction potential is assumed (i.e., $V = 0$). Quantum trajectories are then developed from the guidance condition $p(x, t) = \partial S(x, t)/\partial x$, which defines the *quantum momentum function* (QMF). By analytical continuation, the x variable is extended to the complex plane through the $z = x + iy$ complex variable (time remains real-valued) and complex quantum trajectories are determined from $p(z, t) = \partial S(z, t)/\partial z = (\hbar/i) \partial \ln \Psi(z, t)/\partial z$. Two kinds of singularities are especially relevant: (i) *nodes* of the wave function, which correspond to *poles* of the QMF, and (ii) *stagnation points* [74, 75], which occur where the QMF is zero and correspond to points where the first derivative of the wave function is also zero.

The local topology for complex quantum streamlines around nodal and stagnation points will be determined at each time and this leads to the concept of quantum caves. Although the QMF displays hyperbolic flow around a node, its Pólya vector field displays circular flow near a node. We can also determine Pólya trajectories from $dz/dt = P(z, t)/m$, where $P(z, t)$ is the Pólya vector field and it is given by the complex conjugate of the QMF, $P(z, t) = \bar{p}(z, t)$. This new vector field provides a simple geometrical and physical interpretation for complex circulation integrals

$$\Gamma = \oint_C p(z) dz = \oint_C \mathbf{P} \cdot d\mathbf{l} + i \oint_C \mathbf{P} \cdot d\mathbf{n} \quad (2.37)$$

where C denotes a simple closed curve in the complex plane, $\mathbf{P} = (p_x, -p_y)$ is the Pólya vector field, $d\mathbf{l} = (dx, dy)$ is the tangent vector in the direction of the path C and $d\mathbf{n} = (dy, -dx)$ is the normal vector pointing to the right as we travel along C . The real part of the circulation integral gives the total amount of work done in moving a particle along a close contour C subject to the vector field \mathbf{P} , while the imaginary part gives the total flux of the vector field across the closed contour [76].

As has been shown [61, 62], unfolding of the dynamics from real space into the complex plane yields unexpected and surprising features, including the so-called quantum caves. A deeper analysis of this behavior also leads to the concept of interference lifetime.

2.6 Young's Two-Slit Experiment

2.6.1 Interference and Boundary Effects

In Sect. 1.4 we have considered a simplified simulation of quantum diffraction, assuming that the initial wave function resulted from the effect produced by the diffracting object (in that case, a single aperture) on some incoming wave function. This fact stresses the direct connection between diffraction and boundary conditions. In Young's two-slit experiment, this combination results particularly interesting: the superposition of the two waves coming from each slit give rise to an interference pattern, which is modulated by the diffraction pattern associated with these slits.

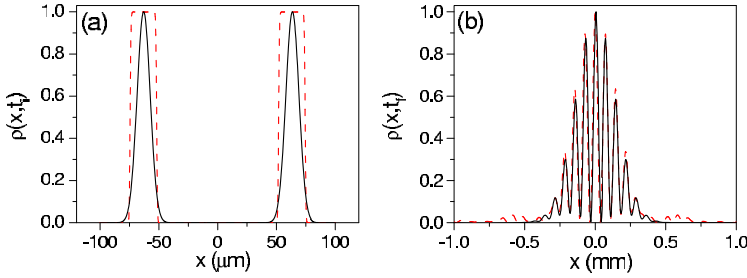


Fig. 2.14 (a) Initial probability densities associated with hard-wall slits (*dashed red line*) and Gaussian slits (*black solid line*). (b) Young-type probability density patterns produced by the interference of the wave packets illustrated in panel (a) at a flight distance $z_f = 5$ m

Something similar also happens with multiple-slit gratings, where other interesting phenomena appear, but this will be seen in next chapter.

In order to illustrate the relationship between diffraction and boundary effects in Young's two-slit experiment, we are going to consider hard-wall slits, as in Sect. 1.4, using as working parameters those provided by Zeilinger *et al.* [16] for two-slit interference with slow neutrons. In this case, the de Broglie wavelength was $\lambda = 18.45 \text{ \AA}$, which means an associated (subsonic) velocity $v = 214.4 \text{ ms}^{-1}$ and a total time of flight $\tau_f = 2.26 \times 10^{-2} \text{ s}$ (detectors are placed at a distance of 5 m from the screen containing the two slits). Regarding the two slits, the width for both slits is $w = 22.2 \mu\text{m}$ (we assume identical slits; for nonidentical ones, go to Sect. 2.6.3), and the distance between their centers is $d = 126.3 \mu\text{m}$ (the separation between the inner borders of the slits is $104.1 \mu\text{m}$). As for the initial wave functions, we have considered two types. One assumes that the slits are described by hard-walls, with total transmission along their widths and zero everywhere else. Therefore, the transmitted (initial) wave functions are quasi-plane waves along the x -direction and a relatively wide Gaussian wave packet along the z -direction, just as in Sect. 1.4, although taking into account that now we have a coherent superposition of two of such wave packets. In the other case, the slits are assumed to have a Gaussian transmission, thus producing Gaussian wave packets. These wave packets have the same width along the z -direction than the previous ones, and along the x -direction their width is $\sigma_{0,x} = w/4$, such that only a tiny tail goes beyond the boundaries of the (hard-wall) slits (the probability associated with these tails is meaningless). The corresponding initial probability densities are displayed in Fig. 2.14(a).

When the wave functions considered are let to freely evolve until their centroids in the z -direction reach the final or *flight* distance $z_f = 5$ m, the interference patterns that we find along the x -direction are those displayed in Fig. 2.14(b). As it can be noticed, the interference pattern (along the x -direction) associated with the hard-wall slits is in agreement with the two-slit interference formula for this type of slit in the Fraunhofer regime [77],

$$\rho_{x,\infty}(x) = |\Psi_{x,\infty}(x)|^2 \sim \left[\frac{\sin(\pi w x / \lambda z_f)}{\pi w x / \lambda z_f} \right]^2 \cos^2(\pi d x / \lambda z_f). \quad (2.38)$$

That is, we have interference fringes of width $\delta x = \lambda z_f / d = 73 \mu\text{m}$ and centered at $x_n = n\lambda z_f / d$, with $n = 0, \pm 1, \pm 2, \dots$. These fringes are modulated by the diffraction factor, which displays maxima at $x = 0$ and each time that $x_\ell^{\text{max}} = (\ell + 1/2)\lambda z_f / w$, and minima whenever $x_\ell^{\text{min}} = \ell\lambda z_f / w$. In this sense, notice that if $n/\ell = d/w$, the ℓ th diffraction minimum will cancel out the n th interference fringe. For example, in our case, we have $d/w = 5.69$, which means that the $\ell = 3$ diffraction minimum will almost cancel out the $n = 17$ interference fringe.

In the case of the Gaussian slits, the diffraction envelope is not a sinc-function, but a Gaussian (diffraction by Gaussian slits produces wave functions which remain always Gaussian), as seen in Fig. 2.14(b). This means that the diffraction term in (2.38) has to be replaced by a Gaussian. This Gaussian is given by long-time limit of the probability density associated with the Gaussian wave packet (1.2), centered at $x_0 = 0$ and $p_0 = 0$, and with $\sigma_0 = \sigma_{0,x}$. Thus, the pattern produced by two Gaussian slits is described¹ by

$$\rho_{x,\infty}(x) = |\Psi_{x,\infty}(x)|^2 \sim e^{-x^2/2\bar{\sigma}^2} \cos^2(\pi dx / \lambda z_f), \quad (2.39)$$

where $\bar{\sigma} \equiv \lambda z_f / 4\pi\sigma_0$. Again here the interference orders appear at the same places, since the distance between the centers of the slits has not changed. However, contrarily to what happens with the previous case, the diffraction envelope cancels any interference feature beyond the reach of the Gaussian, i.e., for a few times the width $\bar{\sigma}$ (e.g., for $x = 3\bar{\sigma} \approx 0.4 \text{ mm}$ the probability density is almost vanished).

In order to visualize the process that connects the initial distributions displayed in Fig. 2.14(a) with the corresponding final interference fringes observed in Fig. 2.14(b), in Fig. 2.15 we show the associated Bohmian trajectories. In the case of hard-wall slits (see Fig. 2.15(a)), we notice how the trajectories with outermost initial conditions (with respect to the margins of the slits) undergo a faster transversal motion (see the enlargement of the Fresnel regime in Fig. 2.15(b)), thus leading to a faster overlapping between the two outgoing or diffracted waves than in the Gaussian case. In this latter case, represented in Fig. 2.15(c), single-slit diffraction proceeds more slowly and gradually, as seen in Fig. 2.15(d). Actually, this is the reason why the reach of the outermost Bohmian trajectories is much shorter than in the previous case and, eventually, why the associated interference pattern decreases monotonically to zero as the distance from $x = 0$ increases: there are no trajectories than can travel further away, as in the case of the hard-wall slits.

2.6.2 Realistic Two-Slit Diffraction

In the previous section, the initial wave function was a coherent superposition of the two diffracted wave packets. We have not made any consideration about how these

¹Of course, the same result is obtained if one considers a coherent superposition of two wave packets like (1.2), with the centers at $x_0 = \pm d/2$ and $p_0 = 0$, and the computes the corresponding long-time limit expression.

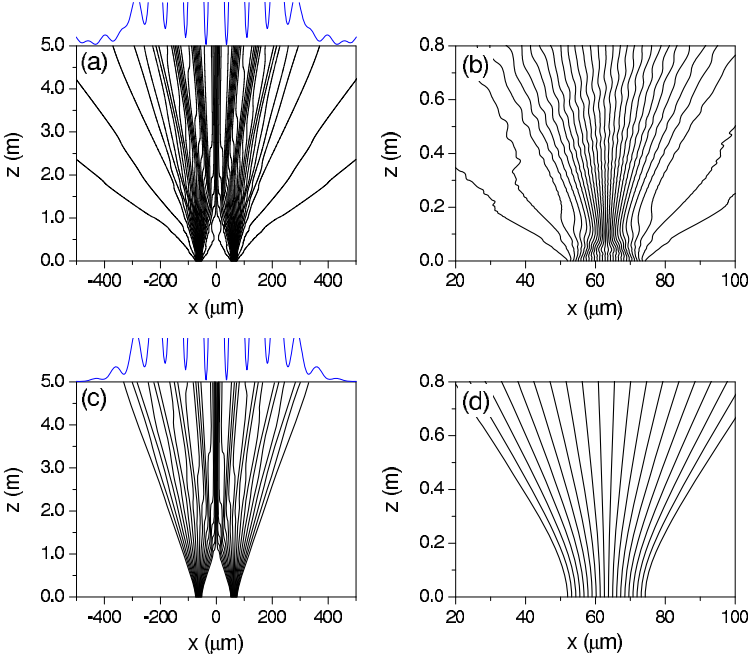


Fig. 2.15 Bohmian trajectories evenly distributed along the two slits for the two cases considered in Fig. 2.14: hard-wall slits (*upper row*) and Gaussian slits (*lower row*). On top of the left-hand side panels, final probability density up to a 10 % of the maximum value. Enlargements showing the Fresnel regime in both cases are shown in the corresponding panels on the right-hand side

two beams appear or how Bohmian trajectories with initial condition $z_0 \neq 0$ behave due to the translational symmetry of the problem. Here we are going to analyze these two effects by means of realistic interactions simulating the slits. In other words, rather than stressing the role of diffraction, here we are going to emphasize that of scattering (the material where the slits are is going to behave as a scattering center). More specifically, we are going to consider two cases, regarded as experiments *A* and *B*, describing the scattering (and subsequent diffraction) of electrons by soft potentials modeling the double-slit [78]—these models are more *realistic* than the typical textbook example of hard-wall slits.

The two-slit potential for experiment *A* is given by

$$V(x, z) = \left(V_0 - \frac{1}{2} m \omega^2 z^2 + \frac{m^2 \omega^4 z^4}{16 V_0} \right) e^{-x^2/\alpha^2}, \quad (2.40)$$

a model used in the literature [79–81] to show the advantages of the backward-forward semiclassical initial value representation into the study of *decoherence*. Here, $\alpha = 25$ bohr, $\omega = 600 \text{ cm}^{-1}$, $V_0 = 8000 \text{ cm}^{-1}$, and m is the electron mass. Experiment *B* is described by a modified version of (2.40) that consists in a slight shift forward (with respect to the plane containing the slit) of the central barrier. The

corresponding potential model, introduced by Guantes *et al.* [78] to study the effects of the central barrier on the electron dynamics, is

$$V(x, z) = \frac{m^2 \omega^4 z^4}{16V_0} e^{-x^2/\alpha^2} + V_0 e^{-(x-x_b)^2/\alpha^2 - z^2/\beta^2}, \quad (2.41)$$

with $\beta = 90$ bohr and $x_b = 125$ bohr. Classically, this model presents direct transmission only for high values of the incidence energy, E_i . For lower values of E_i , the two slits become transversal channels that frustrate such a transmission—the electrons can only pass laterally after bouncing several times over the three walls of the arrangement. The results shown here are for a quasi-plane (or quasi-monochromatic) initial wave function with energy $\bar{E} \approx 500 \text{ cm}^{-1}$, for which there is no direct transmission in experiment *B*. This wave function is launched perpendicular to the two-slit from a distance $x_0 = -400$ bohr (far enough from the interaction region of the soft potential).

In Fig. 2.16 we show the probability density after the collision with the two-slit (top), the transmission function² (center), and the intensity pattern that would appear on a screen behind the slits (bottom) for experiments *A* (left) and *B* (right). From the transmission function, a certain delay in reaching the Fraunhofer regime in experiment *B* (0.55 ps vs 0.27 ps for experiment *A*) is noticeable. This delay is caused by the barrier; as the wave function gets into the region $\Sigma := \{0 \lesssim x \lesssim x_b\}$, it becomes highly peaked inside, giving rise to a *temporary trapping* or *resonance*. The portion of the wave packet inside Σ reaches its maximum at $t \approx 0.18$ ps (see Fig. 2.16(e)), and then the resonance begins to *dissipate*, with the probability either flowing backwards or passing through the transversal channels. Observe that the decay of this resonance becomes asymptotically slower after $t \approx 0.28$ ps (thin solid line), thus still remaining for a relatively long time. This manifests as the appearance of a weak peak in each opening of Σ (the three corresponding peaks are enclosed by circles in Fig. 2.16(d)).

Transient quantum trapping is intimately connected to the presence of *transient classical trapping* or classical chaos [78], what demonstrates a high quantum-classical correspondence. The classical values for the transmittance—the fraction of transmitted particles from an ensemble initially covering the same extension along the y -direction as ρ_0 —are 10.48 % for experiment *A* and 4.05 % for experiment *B*. These values are comparable to those obtained quantum-mechanically—the quantum transmittance is the asymptotic value of the transmission function—14.24 % and 4.78 %, respectively. The slight difference is attributed to tunneling (see below) and diffractive effects.

The previous results have been explained by using the standard version of quantum mechanics. However, in our opinion, a deeper understanding of the dynamics can be gained by using Bohmian mechanics. As seen above, electrons undergo a motion similar to that of particles in a classical fluid, manifesting the action of an

²The transmission function is defined here as the probability to localize the electron behind the two-slit: $\mathcal{T}_t = \int_{x_b}^{+\infty} |\Psi_t(x)|^2 dx$ (in experiment *A*, we have assumed $x_b = 0$ bohr).

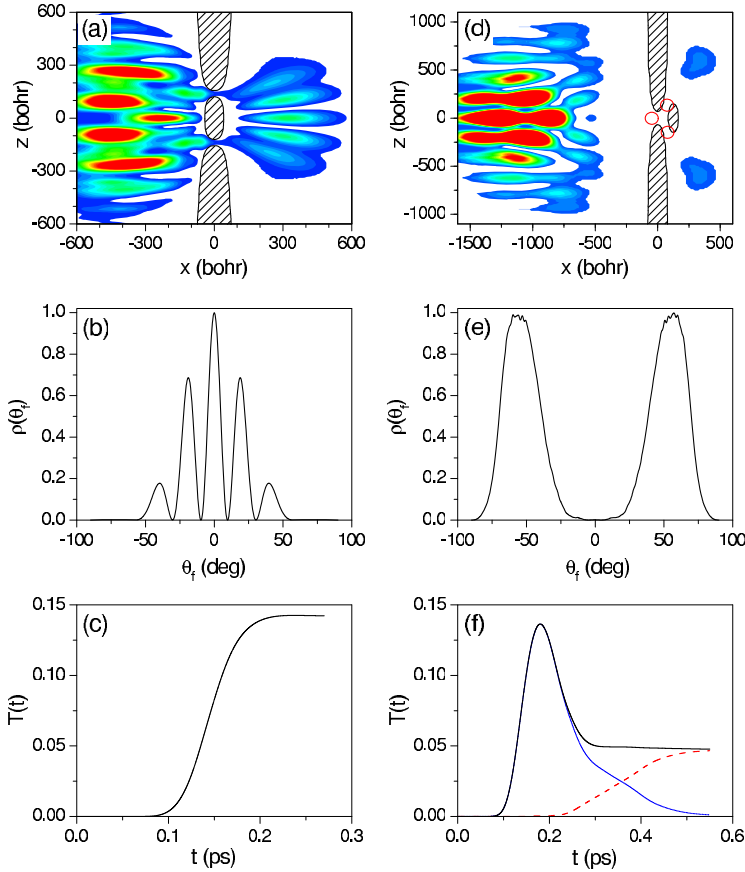


Fig. 2.16 Quantum results for experiments *A* (left) and *B* (right); see text for details: final probability density (top), transmission function (center), and intensity pattern (bottom). In the *uppermost panels*, the initial propagation is from left to right with respect to the plane containing the slits; the *shaded areas* represent a cut of the respective interaction potentials. *Circles* in panel (d) enclose weak resonance peaks. The *thin solid line* in (e) refers to the probability inside Σ , and the *dotted line* denotes the probability behind $x = x_b$

effective potential that is the sum of the classical potential plus the quantum one. The latter, which conveys information on the whole ensemble of particles, gives rise to the quantum pressure. In this way, the electrons with initial positions corresponding to the rear part of ρ_0 (with respect to the direction of propagation) will not be able to reach regions that are accessible to those starting closer to the slits. Indeed, the latter will be “pressed” by those coming behind, being bounded to remain for a longer time in contact with the real two-slit potential. This is something with no analog in the classical problem of a single particle passing through a two-slit.

The aforementioned statements are easily understood by looking at the different ensembles of quantum trajectories plotted in Fig. 2.17. Taking advantage of the

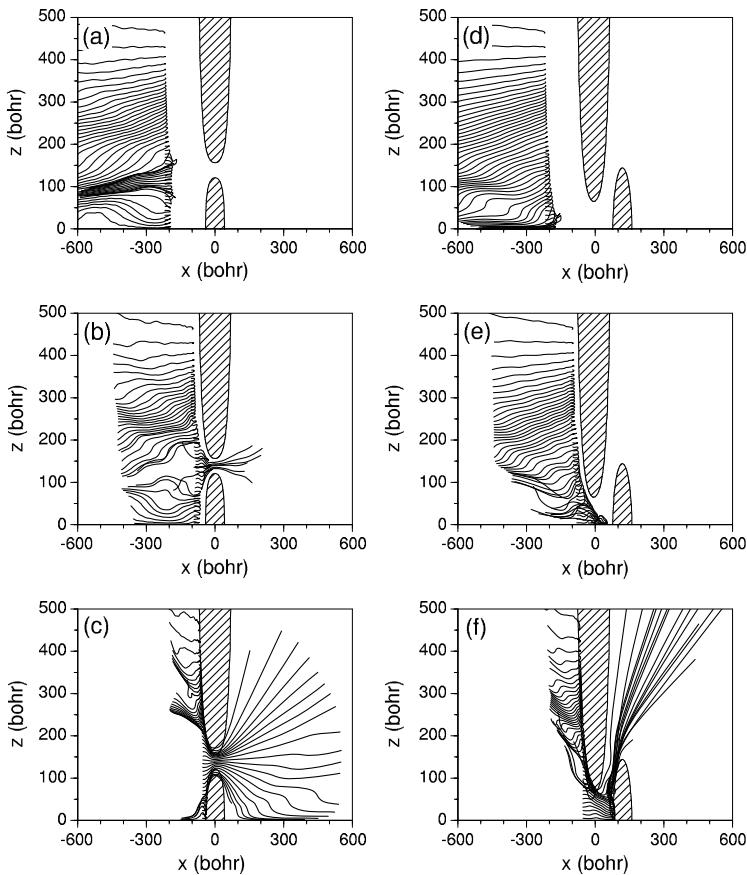


Fig. 2.17 Bohmian trajectories for experiments *A* (left) and *B* (right). The propagation is from left to right with respect to the plane containing the slits, launching the trajectories from: $x(0) = x_0 - 100$ (top), $x(0) = x_0$ (center), and $x(0) = x_0 + 100$ (bottom), with $x_0 = -400$ bohr. For clarity, only the scattered part of half of the trajectories is represented (see text for details); as in Fig. 2.16, the shaded areas represent a cut of the respective interaction potentials

reflection symmetry with respect to $z = 0$, only half of the trajectories (those corresponding to the upper slit) has been represented to make clearer the figures (moreover, the incident part is not shown either). The values of the initial z -coordinate for homologous trajectories in the different panels are the same, and only their initial x -coordinate changes. In particular, three different values of x_0 sampling the three parts of ρ_0 (rear, middle, and front with respect to the direction of propagation, respectively) are considered: $x(0) = x_0 - 100$, $x(0) = x_0$, and $x(0) = x_0 + 100$, with $x_0 = -400$ (all units are given in bohr). As can be seen, the dynamical role of the quantum pressure is fundamental to understand the motion of the electrons. Notice how the trajectories starting at distances further from the two-slit potential (in both experiments) can not reach it, contrary to what happens in a purely classical situ-

ation, where the starting point (provided it is located at asymptotic distances from the potential) does not influence the behavior of subsequent groups of trajectories. Moreover, the distortion that the slits cause on the topology of the trajectories is also remarkable. If the potential was just a wall (i.e., no slits), electrons would get diffracted backwards giving rise to a diffraction pattern similar to that of a wave passing through a two-slit. However, the presence of slits leads to the appearance of some channels (two in experiment *A* and only one in experiment *B*) that disrupt the relatively smooth motion of the reflected electrons.

From a dynamical viewpoint, two interesting effects are worth discussing. First, observe that there is a number of electrons initially starting close to the potential that cannot pass through the slits, but that are pushed away by other particles coming behind. Due to quantum pressure, these electrons have two possibilities to “escape” when are reflected: either by going towards the borders of the incoming wave, or (in the case of experiment *A*; see Fig. 2.17(c)) towards the symmetry axis (i.e., the $z = 0$ axis). Thus, as happens in classical hydrodynamics, here the electrons also move towards those regions where the values of the quantum pressure are smaller. Second, notice the presence of tunneling mentioned above; Figs. 2.17(c) and (f) show how trajectories pass through regions that are classically forbidden. This is possible in Bohmian mechanics because quantum particles have an additional quantum energy arising from the quantum potential [82], which helps them to overcome regions that are classically forbidden. Regarding the conservation of the energy, this does not constitute a problem; quantum-mechanically, the quantity that must be conserved is the average energy of the ensemble, \bar{E} , but *not* the energy of each individual particle.

Although the number of particles passing through the slits is a function of the energy E_0 and the parameters defining the classical potential, it is clear that by studying the electron dynamics one can determine with no ambiguity which part of the initial wave packet is reflected and which one is transmitted. This is something unthinkable in standard quantum mechanics, where the wave function is a kind of “wholeness” from which such an information cannot be inferred. Here, we have seen that the electrons in the rear part of the ensemble do not cross the slits, while those initially closer to the potential do it. That is, the quantum transmittance has contributions from the front of the wave packet, but not from its rear part. Moreover, the electron quantum trajectories also indicates the part of the initial wave packet contributing to each diffraction peak. This fact, as we will see in Sect. 8.5.4, is of capital importance in characterizing diffraction channels in atom-surface scattering.

Finally, let us stress the difference between Figs. 2.17(c) and (f) in relation to Figs. 2.16(c) and (f), respectively. In experiment *A* there is interference of the two diffracted electron beams. This manifests as a kind of “wiggly” behavior in the topology of the trajectories until the electrons reach a diffraction channel or Bragg direction; then, they move as free particles. The formation of these channels in the Fraunhofer region is a direct consequence of the information that the quantum potential transmits to the particles about the status of each slit (either open or close). In the case of experiment *B*, the electrons exiting from each slit behave like if such an information was not relevant, because the diffracted beams do not overlap. This makes electrons to display the free evolution—approximately, since there are still

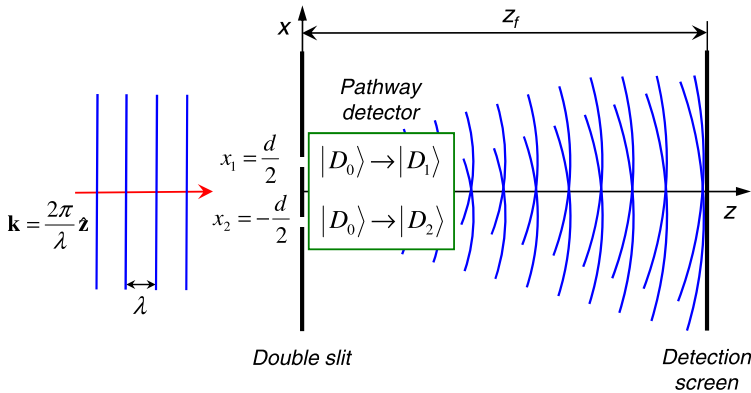


Fig. 2.18 Simple scheme depicting a two-slit experiment with “which-way” detectors behind the slits. These detectors work in such a way that, if a particle passes through the slit at x_{0i} ($i = 1, 2$), its quantum state switches from $|D_0\rangle$ to $|D_i\rangle$

small disturbances produced by the remaining transiently trapped wave—that would correspond to motion under the guidance of a Gaussian wave packet.

2.6.3 Decoherence and Contextuality

The quantum version of Young’s two-slit experiment is used to show the dual nature of massive particle at a microscopic scale. That is, particles behave like localized corpuscles if one “looks” at the slits in order to ascertain the particle’s pathway, and like (delocalized) waves if both slits are unobserved [59]. The unavailability to observe both behaviors at once is known as *complementarity*. Passing from one to another and vice versa by marking or “erasing” the pathway followed by the particle (i.e., the so-called *which-way* information) is known as *quantum eraser experiment* [83]. All these concepts are strongly connected to the emergence of classicality in quantum mechanics and decoherence. Although we are not going to analyze them in depth here, it is interesting at least to catch a glimpse of them.

Thus, consider the simple two-slit setup displayed in Fig. 2.18, which schematically represents the same type of experiment described with hard-wall slits in Sect. 2.6.1 and is quite common in theoretical studies of visibility in two-slit double-slit experiments [84]. To be more specific, let us assume that the two slits are on the XY -plane, at $z = 0$, and placed at $x_{01} = d/2$ and $x_{02} = -d/2$, respectively, being infinitesimally narrow and parallel to the y -axis. The slits are assumed to extend infinitely along to the y -axis, which allows us to further simplify the description and reduce it to the XZ -plane due to translational symmetry along the y -direction. Finally, we assume the hard-wall approximation by neglecting the interaction between the atoms which constitute the grating and the diffracted ones [20, 85, 86], so that there is full transmission along both slit widths and zero transmission everywhere

else. This means that the (overall) advance of the wave function is going to be along the z -direction, while diffraction and interference features will take place essentially along the x -direction.

As in Sect. 2.6.1, the initial wave function is described by a coherent superposition of the position eigenstates $|x_1\rangle$ and $|x_2\rangle$,

$$|\Psi(0)\rangle = \frac{1}{\sqrt{2}}(|x_1\rangle + |x_2\rangle). \quad (2.42)$$

Physically, these position eigenstates represent generic diffracting waves coming out from either slit 1 or slit 2, regardless of the particular form that these waves may display. After passing through the slits, the particle undergoes free, unitary time-propagation until reaching the detection screen, at t . The propagator describing this process is given by $\hat{U}(t, 0) = e^{-i\hat{p}^2 t/2m\hbar}$. Hence the final wave function at the detection screen reads as

$$\begin{aligned} |\Psi(t)\rangle &= \frac{1}{\sqrt{2}}\hat{U}(t, 0)(|x_1\rangle + |x_2\rangle) \\ &= \frac{1}{\sqrt{2}} \int |x\rangle \langle x| U(t, 0)(|x_1\rangle + |x_2\rangle) dx \\ &= \frac{1}{\sqrt{2}} \int_{-\infty}^{\infty} [\psi_1(x, t) + \psi_2(x, t)] |x\rangle dx, \end{aligned} \quad (2.43)$$

where

$$\psi_i(x, t) = \langle x|U(t, 0)|x_i\rangle \propto e^{im(x-x_{0i})^2/2\hbar t} \quad (2.44)$$

is the probability amplitude for the particle to be detected at x (at the scanning screen) given that it passed through slit i at $t = 0$. If the momentum along the propagation direction or longitudinal momentum, $p_z = \hbar k$, remains nearly constant throughout the full propagation, the time elapsed to go from the two slits to the detection screen will be $t = mz_f/p_z = mz_f/\hbar k$, with $k = 2\pi/\lambda$, in agreement with the relation (1.34). Taking this into account, (2.44) can be recast as

$$\psi_i(x, t) \propto e^{ik(x-x_{0i})^2/2z_f}. \quad (2.45)$$

Substituting now the amplitude (2.45) into (2.43), we find the probability density to detect the particle at x on the detection screen,

$$\begin{aligned} |\Psi(x, t)|^2 &= \frac{1}{2} [|\psi_1(x, t)|^2 + |\psi_2(x, t)|^2 + 2\text{Re}\{\psi_1^*(x, t)\psi_2(x, t)\}] \\ &\sim 1 + \cos\left(\frac{2\pi dx}{\lambda z_f}\right). \end{aligned} \quad (2.46)$$

Notice that this factor is the same that we already found in (2.38) and (2.39) accounting for interference, although written in the more compact form $\cos^2(\pi dx/\lambda z_f)$.

Here we have expressed it explicitly in a less compact form in order to better understand the effect of the “which-way” detectors (see below). Regarding the diffraction factor, here it is just a constant, because now the slits are assumed to be infinitesimally narrow, i.e., Dirac δ -functions.

Next we introduce a pathway detector behind the slits in such a way that it couples to the particle (here, we do not care how this specifically happens) as soon as it gets diffracted by one of the slits, as illustrated in Fig. 2.18. That is, at $t = 0$, the pathway detector is assumed to be in a pure state $|D_0\rangle$, and as soon as the particle passes through one or the other slit, the detector state switches to $|D_i\rangle$. Accordingly, initially we express the total (particle plus detector) wave function as

$$|\Psi(0)\rangle = \frac{1}{\sqrt{2}} \int_{-\infty}^{\infty} [\psi_1(x) + \psi_2(x)] |x\rangle dx \otimes |D_0\rangle, \quad (2.47)$$

which is a direct product state of the wave functions describing each subsystem, i.e., it is *factorizable*. Now, once the particle passes through the detector, this wave function is not *factorizable* anymore, but describes an entangled state,

$$|\Psi(t)\rangle = \frac{1}{\sqrt{2}} \int_{-\infty}^{\infty} [\psi_1(x) |D_1\rangle + \psi_2(x) |D_2\rangle] |x\rangle dx. \quad (2.48)$$

Proceeding as before, we find that the probability density describing the particle at x on the screen reads as

$$\begin{aligned} |\Psi(x, t)|^2 &= \frac{1}{2} [|\psi_1(x)|^2 + |\psi_2(x)|^2 + 2\text{Re}\{\psi_1^*(x)\psi_2(x)\langle D_1|D_2\rangle\}] \\ &\propto 1 + \Lambda \cos\left(\frac{2\pi dx}{\lambda z_f} + \varphi_D\right), \end{aligned} \quad (2.49)$$

where the extra factor $\langle D_1|D_2\rangle = \Lambda e^{i\varphi_D}$ in the first line of (2.49) induces, in general, two effects with respect to the unperturbed system: (i) a reduction of the fringe visibility Λ and (ii) a phase-shift φ_D in the original interference pattern. This particular type of damping of the interference fringes or *dephasing* caused by the action of *pointer states* associated with a detector is what we usually regard as *decoherence*. Nonetheless, it is common to exchange the terms dephasing and decoherence even if the elements causing the loss of quantumness in the system are not pointer states, but any general *environment* or *thermal bath*. In any case, notice that if the pathway detector states become orthogonal very quickly, the interference term can even cancel out totally [87].

In Sect. 2.8 we will come back to the issue of decoherence in two-state superpositions—the so-called *Schrödinger cats*—but now we are going to analyze the process of loss of fringe visibility from a Bohmian viewpoint. In this regard, instead of considering the full wave function, we are going to consider some simple models. In this regard, we are going to reconsider again as a working model the interference experiments with slow neutrons carried out by Zeilinger *et al.* [16]. This

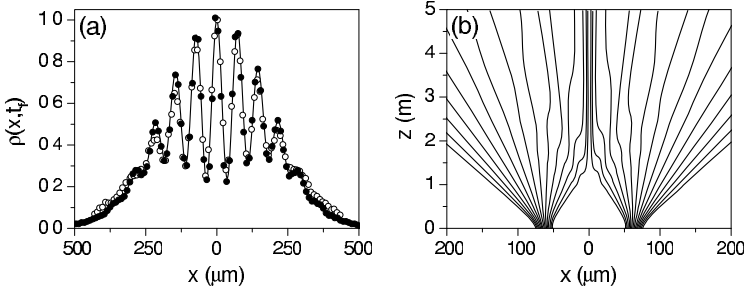


Fig. 2.19 (a) Two-slit interference pattern for slow neutrons [16]: experimental data (*open circles*), standard quantum results obtained with (2.51) (*solid line*), and Bohmian statistical results obtained from (2.52) (*full circles*). (b) Sample of Bohmian trajectories illustrating the dynamics associated with the results shown in part (a)

time, we are going to assume that the slits are not symmetric, but with slightly different widths, just as in the real experiment. By means of a thorough analysis, it was seen [88] that the experiment could be affected by decoherence apart from some incoherence associated with the experimental setup itself (slit arrangements and beam collimation). Accordingly, the experiment could be described by a model similar to the one leading to (2.49), where each diffracted wave function was assumed to be Gaussian-like, as described in Sect. 2.6.1, but with different widths, and the fringe visibility or coherence degree function depended on time as

$$\Lambda_t = \text{sech}(t/\tau_c), \quad (2.50)$$

with $\tau_c = 2.33 \times 10^{-2}$ s being the coherence time determined empirically from the experimental results. This ratio came from the assumption that the environment states displayed an exponentially decaying overlapping with time [87], i.e., $\alpha_t = \langle D_2 | D_1 \rangle \sim e^{-t/\tau_c}$, with meaningless phase-shift, φ_D . This gradual decrease with time is associated with the fact that, rather than pointer states, the loss of fringe visibility would arise from the interaction of the neutrons with an environment between the slits and the detection screen. In Fig. 2.19(a) we observe the agreement between the experimental results (open circles) and this simple model (solid line) [88, 89], where the latter is accounted for by

$$\tilde{\rho}^2(x, t) \propto |\psi_1(x, t)|^2 + |\psi_2(x, t)|^2 + 2\Lambda_t |\psi_1(x, t)| |\psi_2(x, t)| \cos \delta_t, \quad (2.51)$$

which is essentially the same as (2.49), but associating a particular width to each intensity term. More specifically, here ψ_i denotes the diffracted Gaussian wave packet coming out from the i th slit and δ_t is the time-dependent phase associated with the two wave-packet interference; the ‘tilde’ over ρ indicates that this quantity is the *reduced* probability density, i.e., the probability density that results when we trace over the environment ($|D_1\rangle, |D_2\rangle$) degrees of freedom and look only at the system’s behavior, as defined by (6.93) (see Sect. 6.3.4, Vol. 1).

As also shown in Sect. 6.3.4 (Vol. 1; notice that several equations from this section are called here, below), a reduced probability density like (2.51) satisfies a continuity equation given by (6.95), from which we define a reduced quantum current density (6.94), the corresponding flux (6.96) and, therefore, the associated reduced Bohmian trajectories (6.97). When this formulation is applied to this model [89], the corresponding equation of motion reads as

$$\begin{aligned} \dot{\mathbf{r}} = & \frac{(1 + |\alpha_t|^2)\hbar}{2im\tilde{\rho}} \sum_{j=1}^2 |c_j|^2 [\psi_j^* \nabla \psi_j - \psi_j \nabla \psi_j^*] \\ & + \frac{\hbar}{im\tilde{\rho}} \alpha_t c_1 c_2^* [\psi_2^* \nabla \psi_1 - \psi_1 \nabla \psi_2^*] + c.c., \end{aligned} \quad (2.52)$$

where “*c.c.*” refers to the conjugate complex of the preceding term on the same line of the equation. A sample of trajectories obtained integrating this equation can be seen in Fig. 2.19(b), while a full statistical calculation is displayed in panel (a), where we find the agreement with both the experiment and the simple model represented by (2.51). Notice that the correspondence between the trajectories and the latter result constitute an empirical proof of the reduced continuity equation (6.95) and the quantum flux transport condition (6.96).

As seen in Fig. 2.19(b), although decoherence induces some quenching of the interference fringes, we still observe the survival of a very important quantum trait associated with interference, namely the non-crossing property of the quantum flux. In a classical-like situation or, in other words, under severe “which-way” information conditions, when we have lost any interference feature, one would expect to observe that these trajectories cross. If we examine more closely (2.52), we notice that in the limit of total loss of coherence, i.e., for very large τ_c ($\tau_c \gg \tau_f$), so that α_t vanishes very quickly, this equation becomes

$$\dot{\mathbf{r}} = \frac{|c_1|^2 \rho_1 \dot{\mathbf{r}}_1 + |c_2|^2 \rho_2 \dot{\mathbf{r}}_2}{\rho_{cl}}, \quad (2.53)$$

with

$$\rho_{cl} \equiv |c_1|^2 \rho_1 + |c_2|^2 \rho_2. \quad (2.54)$$

Thus, although the total probability density is classical like, as well as it also happens with the corresponding quantum probability current density,

$$\mathbf{J}_{cl} \equiv \rho_{cl} \dot{\mathbf{r}} = |c_1|^2 \rho_1 \dot{\mathbf{r}}_1 + |c_2|^2 \rho_2 \dot{\mathbf{r}}_2 \quad (2.55)$$

i.e., both respect the law of addition of probabilities—the trajectories still satisfy the non-crossing property, because they contain information about the fact that *both* slits are open simultaneously. We can observe these two non-exclusive behaviors in Fig. 2.20: although statistically we reproduce the expected classical-like results, the trajectories behave in a rather non-classical fashion.

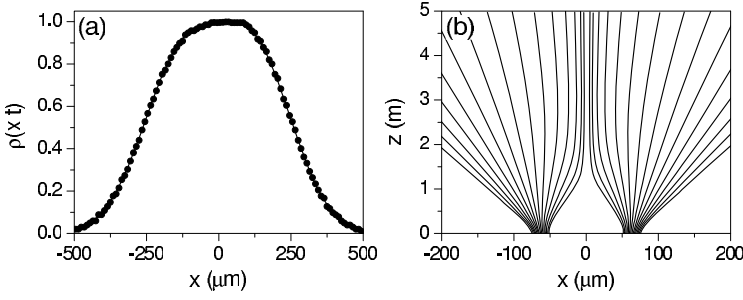


Fig. 2.20 (a) Two-slit interference pattern for slow neutrons [16] with $\tau_c \gg \tau_f$: standard quantum results obtained with (2.51) (solid line), and Bohmian statistical results obtained from (2.52) (full circles). (b) Sample of Bohmian trajectories illustrating the dynamics associated with the results shown in part (a)

In order to better understand the above non-violation of the crossing property, notice that in the previous example we have analyzed an overall quantum flow, without having into account that part of the system coherence can flow towards the environment. In this sense, more refined higher-dimensional models can be used to analyze this effect [90–94], as well as simpler ones based on conditional wave functions [95–98] or hybrid Bohmian-classical approaches (see Sect. 6.3.3, Vol. 1), in the spirit of the Born-Oppenheimer approximation (see Sect. 8.2). Alternatively, we can also consider another simple model to describe the transition from a context with total information about the two slits to another one where this information is completely removed or *erased* [99]. In principle, the classical-like situation appears if the information about the slits not crossed by the particle disappears or is, somehow, screened. Therefore, one could think of a certain *screening time*, τ_s , which provides a time scale on how fast the information about the non-crossed slit disappears. In a strict sense, in principle this information cannot be disentangled from the one referring to the loss of coherence. However, as we are going to see, analyzing the two-slit experiment in this way results very insightful.

Thus, consider that the aforementioned “which-way” information decays exponentially. That is, if the particle passes through slit 1, for example, the coefficient associated with ψ_2 will display a time-dependence $c_{l2} = c_{02}e^{-t/\tau_s}$, while the coefficient for ψ_1 will be

$$c_{l1} = c_{01}\sqrt{1 - |c_{02}|^2 e^{-2t/\tau_s}}, \quad (2.56)$$

which means that the information about the passage through the slit 1 increases or is enhanced in a similar proportion to the decrease of the information about slit 2. The corresponding trajectories are obtained by substituting the explicit expressions for c_{l1} and c_{l2} into (2.53). Taking this into account, if $\tau_s \ll \tau_c$, the screening of the empty-slit information takes place much faster than the process that leads to the quenching or damping of the interference fringes. In this case, if the screened slit

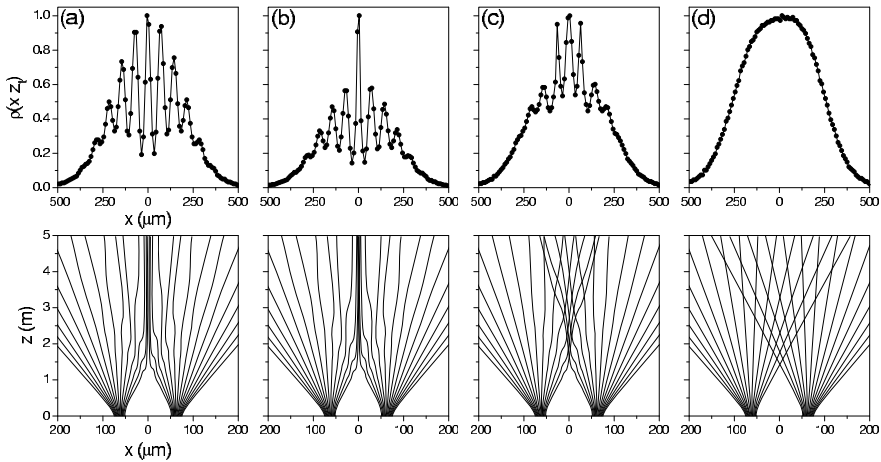


Fig. 2.21 *Top:* Probability density (full circles) obtained after counting the corresponding modified reduced Bohmian trajectories for: (a) $\tau_s \ll \tau_c$, (b) $\tau_s = 10\tau_c$, (c) $\tau_s = \tau_c$, and (d) $\tau_s = 0.1\tau_c$. For a better visualization, the results have been joined by means of B-splines (solid line). *Bottom:* Samples of trajectories illustrating the dynamics of the results shown in the upper panels

is 2, for example, (2.53) reduces to

$$\dot{\mathbf{r}} = \dot{\mathbf{r}}_1 \quad (2.57)$$

and the trajectories will evolve like if there was no other slit at all—i.e., just as if we would be dealing with a context where there is only one slit open at a time. Now particles are allowed to violate the non-crossing property, because the Bohmian momentum at a particular point of configuration space may acquire any value (as in classical mechanics). The behavior of the probability densities (top) and the associated modified reduced Bohmian trajectories (bottom) for different values of the ratio τ_s/τ_c are displayed in Fig. 2.21, ranging from the situation described with the previous model to a typical classical-like context (from left to right). As it can be noticed by comparing with more realistic higher-dimensional models [90–94], the behavior displayed by the trajectories here resembles quite remarkably the one shown by the trajectories in such models, even though the latter is only apparent, since the high-dimensional trajectories never cross, but only their projections in the particle’s configuration subspace.

2.7 Dissipation Effects

As in Sect. 1.6, now we are going to consider the case of a coherent superposition of two Gaussian wave packets—like the one accounted by (2.3), but with $c_1 = c_2$ —acted by a (quantum) viscous medium [100]. Each wave packet then evolves according to (1.42). Taking this into account, it can be readily shown that the associated Bohmian equation of motion can be expressed as

$$\begin{aligned}
\dot{x} &= \frac{\rho_1}{\rho} \dot{x}_1 + \frac{\rho_2}{\rho} \dot{x}_2 + \frac{\hbar e^{-\gamma t}}{m\rho} \operatorname{Im} \left(\psi_1^* \frac{\partial \psi_2}{\partial x} - \psi_2 \frac{\partial \psi_1^*}{\partial x} \right) \\
&= \frac{\rho_1}{\rho} \left[\frac{p_{t1}}{m} + \frac{2 \operatorname{Re}(\alpha_{t1})}{m} e^{-\gamma t} (x - x_{t1}) \right] \\
&\quad + \frac{\rho_2}{\rho} \left[\frac{p_{t2}}{m} + \frac{2 \operatorname{Re}(\alpha_{t2})}{m} e^{-\gamma t} (x - x_{t2}) \right] \\
&\quad + 2 \cos \beta_{12} \frac{\sqrt{\rho_1 \rho_2}}{\rho} \left(\frac{p_{t1} + p_{t2}}{2m} \right) \\
&\quad + 2 \cos \beta_{12} \frac{\sqrt{\rho_1 \rho_2}}{\rho} \left[\frac{\operatorname{Re}(\alpha_{t1})(x - x_{t1}) + \operatorname{Re}(\alpha_{t2})(x - x_{t2})}{m} \right] e^{-\gamma t} \\
&\quad - 2 \sin \beta_{12} \frac{\sqrt{\rho_1 \rho_2}}{\rho} \left[\frac{\operatorname{Im}(\alpha_{t1})(x - x_{t1}) - \operatorname{Im}(\alpha_{t2})(x - x_{t2})}{m} \right] e^{-\gamma t}. \quad (2.58)
\end{aligned}$$

Here, $\beta_{12} = (S_1 - S_2)/\hbar$, with ρ_i and S_i ($i = 1, 2$) being the probability density and real phase associated with i th wave packet when expressed in polar form. Depending on the value assigned to the parameters of each wave packet, different dynamics can be generated. For example, if they have the same width ($\alpha_{t1} = \alpha_{t2} = \alpha_t$) and are located at symmetric positions with respect to $x = 0$ ($x_{t1} = x_0 = -x_{t2}$), (2.58) reduces to

$$\begin{aligned}
\dot{x} &= \frac{\rho_1}{\rho} \left[\frac{p_{t1}}{m} + \frac{2 \operatorname{Re}(\alpha_t)}{m} e^{-\gamma t} (x - x_0) \right] + \frac{\rho_2}{\rho} \left[\frac{p_{t2}}{m} + \frac{2 \operatorname{Re}(\alpha_t)}{m} e^{-\gamma t} (x + x_0) \right] \\
&\quad + 2 \cos \beta_{12} \frac{\sqrt{\rho_1 \rho_2}}{\rho} \left\{ \frac{p_{t1} + p_{t2}}{2m} + \frac{2 \operatorname{Re}(\alpha_t)}{m} e^{-\gamma t} x \right\} \\
&\quad + 2 \sin \beta_{12} \frac{\sqrt{\rho_1 \rho_2}}{\rho} \left[\frac{2 \operatorname{Im}(\alpha_t)}{m} e^{-\gamma t} x_0 \right]. \quad (2.59)
\end{aligned}$$

If now we assumed no translational momentum (i.e., $p_{01} = p_{02} = 0$), this expression can be further simplified and becomes

$$\begin{aligned}
\dot{x} &= \frac{\rho_1}{\rho} \left[\frac{2 \operatorname{Re}(\alpha_t)}{m} e^{-\gamma t} (x - x_0) \right] + \frac{\rho_2}{\rho} \left[\frac{2 \operatorname{Re}(\alpha_t)}{m} e^{-\gamma t} (x + x_0) \right] \\
&\quad + 2 \cos \beta_{12} \frac{\sqrt{\rho_1 \rho_2}}{\rho} \left[\frac{2 \operatorname{Re}(\alpha_t)}{m} e^{-\gamma t} x \right] \\
&\quad + 2 \sin \beta_{12} \frac{\sqrt{\rho_1 \rho_2}}{\rho} \left[\frac{2 \operatorname{Im}(\alpha_t)}{m} e^{-\gamma t} x_0 \right]. \quad (2.60)
\end{aligned}$$

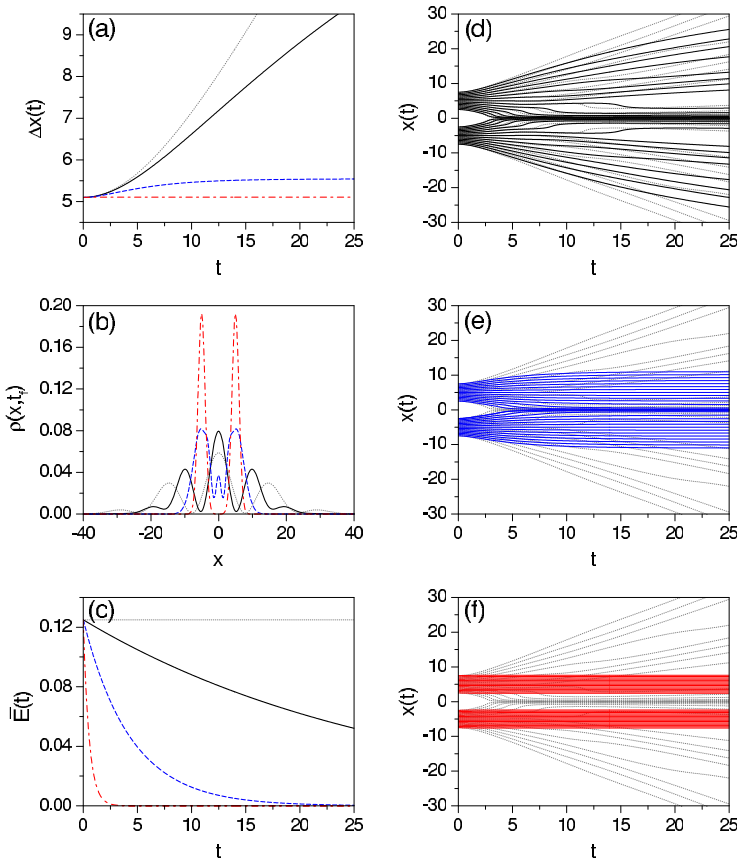


Fig. 2.22 *Left: (a) Position dispersion, (b) final probability density, and (c) energy expectation value for a coherent superposition of two Gaussian wave packets in a viscous medium: $\gamma = 0.035$ (solid black line), $\gamma = 0.23$ (blue dashed line), and $\gamma = 1.84$ (red dashed-dotted line). To compare with, the corresponding frictionless ($\gamma = 0$) quantities are also included (gray dotted line). Right: Dissipative Bohmian trajectories for: (a) $\gamma = 0.035$, (b) $\gamma = 0.23$, and (c) $\gamma = 1.84$. The frictionless, standard Bohmian trajectories ($\gamma = 0$) have also been represented with gray for comparison. The value of the parameters considered in these simulations are: $x_0 = 5$, $\sigma_0 = 1$, $m = 1$, and $\hbar = 1$*

In Fig. 2.22 we show a series of results illustrating the dynamics of this kind of superpositions under the influence of a viscous medium for different values of the friction constant, γ . In particular, in the upper panels we show the position dispersion $\Delta x = \sqrt{\langle x^2 \rangle - \langle x \rangle^2}$ (a), the final probability density (b), and the energy expectation value. As it can be seen, as γ increases, the localization produced on each of the wave packets (see panel (a)) makes that they cannot interfere and therefore the pattern disappears in detriment of two localized Gaussian distributions (see panel (b)). To compare with, the corresponding frictionless quantities are also displayed (gray dotted lines). This friction dynamics becomes more apparent when we

look at the corresponding dissipative Bohmian trajectories, shown in the right-hand side panels (from top to bottom, increasing values of γ ; the frictionless, standard Bohmian trajectories are also represented for comparison). The sets of selected trajectories allow us to notice how the friction of the medium leads to the localization of the two wave packets by gradually “freezing” them. Nonetheless, we would like to note that, contrary to the effects observed with the simplified decoherence models of Sect. 2.6.3, here the reason why there is no interference is because the wave packets cannot see each other rather than because the destruction (over time) of their mutual coherence.

2.8 Quantum Stochastic Trajectories. Schrödinger Cat States

In Sect. 1.4 we have introduced the notion of quantum stochastic trajectory within the context of the stochastic evolution of a free wave packet. More specifically, we considered as a working model the evolution of a free wave packet on a two-dimensional flat surface at a given temperature and with friction. As pointed out, the corresponding quantum trajectories are issued from solving the associated (quantum) Newton equation of motion (1.124). The quantum potential was also obtained after identifying the probability to find a particle at a given position on the surface to the probability density, as shown in (1.125).

Such an analysis can also be extended to the so-called Schrödinger cat states, which may represent the motion of a particle on a two-dimensional surface, with the particle being described by an initial coherent superposition of two well separated Gaussian wave packets. In this problem, one of the main issues is the maintenance of coherence along time. A similar analysis was carried out previously by Ford *et al.* [101–103], but with the purpose of simulating Young’s two-slit experiment in one dimension. For analytical convenience, the surface will be assumed to be one dimensional—generalization to two free wave packets in a two-dimensional surface is straightforward.

Taking this into account, the initial superposition is written as

$$\begin{aligned} \Psi(x, 0) = & \left(\frac{1}{2\pi\sigma_0^2} \right)^{1/4} \frac{1}{\sqrt{2(1 + e^{-d^2/8\sigma_0^2})}} \\ & \times \left[e^{-(x-d/2)^2/4\sigma_0^2 + imv_0x/\hbar} + e^{-(x+d/2)^2/4\sigma_0^2 + imv_0x/\hbar} \right], \quad (2.61) \end{aligned}$$

where σ_0 is the initial width of the Gaussian wave packet, d is the separation between the centers of the two wave packets, and v_0 and m are the particle velocity and mass, respectively. Assuming the particle is in thermal equilibrium and weakly coupled to the environment, the corresponding probability distribution as a function of time is given by

$$P(x, t) = \frac{1}{\sqrt{2\pi\omega^2}} \frac{1}{2(1 + e^{-d^2/8\sigma_0^2})} \left\{ e^{-(x-d/2)^2/2\omega^2} + e^{-(x+d/2)^2/2\omega^2} \right\}$$

$$\begin{aligned}
& + 2 \exp \left[-\frac{x^2}{2\omega^2} - \frac{\omega^2 + (k_B T/m)(\hbar t/2m\sigma_0^2)^2 t^2}{[\sigma_0^2 + (\hbar t/2m\sigma_0)^2]\omega^2} \frac{d^2}{8} \right] \\
& \times \cos \left(\frac{\hbar t dx}{4m\sigma_0^2 \omega^2} \right) \Bigg\}, \tag{2.62}
\end{aligned}$$

where the total spreading $\omega(t)$ is given by the contribution of three terms, as seen in Sect. 1.7: the initial spreading, the quantum contribution, and the mean-square displacement. In (2.62) we notice that the probability distribution also consists of three terms. The first two terms correspond to a pair of separate wave packets, each one only affected by its total spreading issued from solving the standard Langevin equation. The third term involves the typical cosine factor associated with interference. An analysis analogous to the one performed in Sect. 1.7 can also be carried out here in terms of the different thermal and time regimes, i.e., high and low temperatures together with short and long times. Moreover, (2.62) can be again identified with the probability density that appears in the expression for the quantum potential (1.125). In the same direction, the corresponding quantum stochastic trajectories could also be obtained by solving the associated (quantum) Newton equation of motion (1.124).

Several features can be extracted from previous studies. For example, as shown by Ford and coworkers [101–103], decoherence can occur at high temperatures in the absence of dissipation and, conversely, it can also take place even at zero temperature, but in presence of dissipation. Within their approach, particle and environment were entangled at all times. The same properties are expected to be observed in the quantum stochastic trajectories and weak values, as mentioned in Sect. 1.9.

References

1. Davisson, C., Germer, L.H.: Diffraction of electrons by a crystal of nickel. *Phys. Rev.* **30**, 705–740 (1927)
2. Davisson, C., Germer, L.H.: Reflection of electrons by a crystal of nickel. *Nature* **119**, 558–560 (1927)
3. Knauer, P., Stern, O.: Intensitätsmessungen an Molekularstrahlen von Gasen. *Z. Phys.* **53**, 766–778 (1929)
4. Estermann, I., Stern, O.: Beugung von Molekularstrahlen. *Z. Phys.* **61**, 95–125 (1930)
5. Estermann, I., Frisch, R., Stern, O.: Monochromasierung der de Broglie-Wellen von Molekularstrahlen. *Z. Phys.* **73**, 348–365 (1931)
6. Jönsson, C.: Elektroneninterferenzen an mehreren künstlich hergestellten Feinspalten. *Z. Phys.* **161**, 454–474 (1961)
7. Jönsson, C.: Electron Diffraction at Multiple Slits. *Am. J. Phys.* **42**, 4–11 (1974), translation prepared by D. Brandt and S. Hirschi
8. Hirschi, S.: Erratum: Electron diffraction at multiple slits [*Am. J. Phys.* **42**, 4 (1974)]. *Am. J. Phys.* **42**, 423 (1974)
9. Donati, O., Missiroli, G.F., Pozzi, G.: An experiment on electron interference. *Am. J. Phys.* **41**, 639–644 (1973)
10. Merli, G., Missiroli, G.F., Pozzi, G.: On the statistical aspect of electron interference phenomena. *Am. J. Phys.* **44**, 306–307 (1976)

11. Matteucci, G., Pozzi, G.: Two further experiments on electron interference. *Am. J. Phys.* **46**, 619–623 (1978)
12. Frabboni, S., Gazzadi, G.C., Pozzi, G.: Young's double-slit interference experiment with electrons. *Am. J. Phys.* **75**, 1053–1055 (2007)
13. Tonomura, A., Endo, J., Matsuda, T., Kawasaki, T., Exawa, H.: Demonstration of single-electron buildup of an interference pattern. *Am. J. Phys.* **57**, 117–120 (1989)
14. Matteucci, G., Pezzi, M., Pozzi, G., Alberghi, G.L., Giorgi, F., Gabrielli, A., Cesari, N.S., Villa, M., Zoccoli, A., Frabboni, S., Gazzadi, G.C.: Build-up of interference patterns with single electrons. *Eur. J. Phys.* **34**, 511–517 (2013)
15. Gähler, R., Zeilinger, Z.: Wave-optical experiments with very cold neutrons. *Am. J. Phys.* **59**, 316–324 (1991)
16. Zeilinger, A., Gähler, R., Shull, C.G., Treimer, W., Mampe, W.: Single- and double-slit diffraction of neutrons. *Rev. Mod. Phys.* **60**, 1067–1073 (1988)
17. Carnal, O., Mlynek, J.: Young's double-slit experiment with atoms: A simple atom interferometer. *Phys. Rev. Lett.* **66**, 2689–2692 (1991)
18. Keith, D.W., Eckstrom, C.R., Turchette, Q.A., Pritchard, D.E.: An interferometer for atoms. *Phys. Rev. Lett.* **66**, 2693–2696 (1991)
19. Cronin, A.D., Schmiedmayer, J., Pritchard, D.E.: Optics and interferometry with atoms and molecules. *Rev. Mod. Phys.* **81**, 1051–1129 (2009)
20. Doak, R.B., Grisenti, R.E., Rehbein, S., Schmahl, G., Toennies, J.P., Wöll, Ch.: Towards realization of an atomic de Broglie microscope: Helium atom focusing using Fresnel zone plates. *Phys. Rev. Lett.* **83**, 4229–4232 (1999)
21. Schöllkopf, W., Toennies, J.P.: Nondestructive massive selection of small van der Waals clusters. *Science* **266**, 1345–1348 (1994)
22. Arndt, M., Nairz, O., Voss-Andreae, J., Keller, C., van der Zouw, G., Zeilinger, A.: Wave-particle duality of C_{60} . *Nature* **401**, 680–682 (1999)
23. Hackermüller, L., Uttenthaler, S., Hornberger, K., Reiger, E., Brezger, B., Zeilinger, A., Arndt, M.: Wave nature of biomolecules and fluorofullerenes. *Phys. Rev. Lett.* **91**, 90408(1–4) (2003)
24. Gerlich, S., Gring, M., Ulbricht, H., Hornberger, K., Tüxen, J., Mayor, M., Arndt, M.: Matter-wave metrology as a complementary tool for mass spectrometry. *Angew. Chem. Int. Ed.* **47**, 6195–6198 (2008)
25. Gerlich, S., Hackermüller, L., Hornberger, K., Stibor, A., Ulbricht, H., Gring, M., Goldfarb, F., Savas, T., Mürri, M., Mayor, M., Arndt, M.: A Kapitza–Dirac–Talbot–Lau interferometer for highly polarizable molecules. *Nat. Phys.* **3**, 711–715 (2007)
26. Andrews, M.R., Townsend, C.G., Miesner, H.-J., Durfee, D.S., Kum, D.M., Ketterle, W.: Observation of interference between two Bose condensates. *Science* **275**, 637–641 (1997)
27. Parker, S.: A single-photon double-slit interference experiment. *Am. J. Phys.* **39**, 420–424 (1971)
28. Parker, S.: Single-photon double-slit interference—A demonstration. *Am. J. Phys.* **40**, 1003–1007 (1972)
29. Rueckner, W., Titcomb, P.: A lecture demonstration of single photon interference. *Am. J. Phys.* **64**, 184–188 (1996)
30. Dimitrova, T.L., Weis, A.: The wave-particle duality of light: A demonstration experiment. *Am. J. Phys.* **76**, 137–142 (2008)
31. Shimizu, F., Shimizu, K., Takuma, H.: Double-slit interference with ultracold metastable neon atoms. *Phys. Rev. A* **46**, R17–R20 (1992)
32. Schrödinger, E.: Discussion of probability relations between separated systems. *Proc. Camb. Philol. Soc.* **31**, 555–563 (1935)
33. Schrödinger, E.: Probability relations between separated systems. *Proc. Camb. Philol. Soc.* **32**, 446–452 (1936)
34. Einstein, A., Podolsky, B., Rosen, N.: Can quantum-mechanical description of physical reality be considered complete? *Phys. Rev.* **47**, 777–780 (1935)
35. Bohm, D.: *Quantum Mechanics*. Dover, New York (1951)

36. Macchiavello, C., Palma, G.M., Zeilinger, A. (eds.): Quantum Computation and Quantum Information Theory. World Scientific, Singapore (1999)
37. Nielsen, M.A., Chuang, I.L.: Quantum Computation and Quantum Information. Cambridge University Press, Cambridge (2000)
38. Feynman, R.P., Leighton, R.B., Sands, M.: Quantum Mechanics. The Feynman Lectures on Physics, vol. 3. Addison-Wesley, Reading (1965)
39. Scalapino, D.J.: The theory of Josephson tunneling. In: Burstein, E., Lundqvist, S. (eds.) Tunneling Phenomena in Solids, pp. 447–518. Plenum Press, New York (1969)
40. Brumer, P.W., Shapiro, M.: Principles of the Quantum Control of Molecular Processes. Wiley-Interscience, Hoboken (2003)
41. Berman, P.R. (ed.): Atom Interferometry. Academic Press, San Diego (1997)
42. Shin, Y., Saba, M., Pasquini, T.A., Ketterle, W., Pritchard, D.E., Leanhardt, A.E.: Atom interferometry with Bose-Einstein condensates in a double-well potential. *Phys. Rev. Lett.* **92**, 050405(1–4) (2004)
43. Zhang, M., Zhang, P., Chapman, M.S., You, L.: Controlled splitting of an atomic wave packet. *Phys. Rev. Lett.* **97**, 070403(1–4) (2006)
44. Cederbaum, L.S., Streltsov, A.I., Band, Y.B., Alon, O.E.: Interferences in the density of two Bose-Einstein condensates consisting of identical or different atoms. *Phys. Rev. Lett.* **98**, 110405(1–4) (2007)
45. Hänsel, W., Reichel, J., Hommelhoff, P., Hänsch, T.W.: Magnetic conveyor belt for transporting and merging trapped atom clouds. *Phys. Rev. Lett.* **86**, 608–611 (2001)
46. Hänsel, W., Reichel, J., Hommelhoff, P., Hänsch, T.W.: Trapped-atom interferometer in a magnetic microtrap. *Phys. Rev. A* **64**, 063607(1–6) (2001)
47. Hinds, E.A., Vale, C.J., Boshier, M.G.: Two-wire waveguide and interferometer for cold atoms. *Phys. Rev. Lett.* **86**, 1462–1465 (2001)
48. Andersson, E., Calarco, T., Folman, R., Andersson, M., Hessmo, B., Schmiedmayer, J.: Multimode interferometer for guided matter waves. *Phys. Rev. Lett.* **88**, 100401(1–4) (2002)
49. Kapale, K.T., Dowling, J.P.: Vortex phase qubit: Generating arbitrary, counterrotating, coherent superpositions in Bose-Einstein condensates via optical angular momentum beams. *Phys. Rev. Lett.* **95**, 173601(1–4) (1995)
50. Thanvanthri, S., Kapale, K.T., Dowling, J.P.: Arbitrary coherent superpositions of quantized vortices in Bose-Einstein condensates via orbital angular momentum of light. *Phys. Rev. A* **77**, 053825(1–13) (2008)
51. Chapman, M.S., Ekstrom, C.R., Hammond, T.D., Schmiedmayer, J., Tannian, B.E., Wehinger, S., Pritchard, D.E.: Near-field imaging of atom diffraction gratings: The atomic Talbot effect. *Phys. Rev. A* **51**, R14–R17 (1995)
52. Deng, L., Hagley, E.W., Denschlag, J., Simsarian, J.E., Edwards, M., Clark, C.W., Helmerston, K., Rolston, S.L., Phillips, W.D.: Temporal, matter-wave-dispersion Talbot effect. *Phys. Rev. Lett.* **83**, 5407–5411 (1999)
53. Sanz, A.S., Miret-Artés, S.: A trajectory-based understanding of quantum interference. *J. Phys. A* **41**, 435303(1–23) (2008)
54. Sanz, A.S., Borondo, F., Miret-Artés, S.: Particle diffraction studied using quantum trajectories. *J. Phys. Condens. Matter* **14**, 6109–6145 (2002)
55. Sanz, A.S., Borondo, F., Miret-Artés, S.: Causal trajectories description of atom diffraction by surfaces. *Phys. Rev. B* **61**, 7743–7751 (2000)
56. Sanz, A.S., Miret-Artés, S.: A causal look into the quantum Talbot effect. *J. Chem. Phys.* **126**, 234106(1–11) (2007)
57. Kocsis, S., Braverman, B., Ravets, S., Stevens, M.J., Mirin, R.P., Shalm, L.K., Steinberg, A.M.: Observing the average trajectories of single photons in a two-slit interferometer. *Science* **332**, 1170–1173 (2011)
58. Wyatt, R.E.: Quantum Dynamics with Trajectories. Springer, Berlin (2005)
59. Schiff, L.I.: Quantum Mechanics, 3rd edn. McGraw-Hill, Singapore (1968)
60. Sanz, A.S., Miret-Artés, S.: Interplay of causticity and vorticality within the complex quantum Hamilton–Jacobi formalism. *Chem. Phys. Lett.* **458**, 239–243 (2008)

61. Chou, C.-C., Sanz, A.S., Miret-Artés, S., Wyatt, R.E.: Hydrodynamic view of wave-packet interference: Quantum caves. *Phys. Rev. Lett.* **102**, 250401(1–4) (2009)
62. Chou, C.-C., Sanz, A.S., Miret-Artés, S., Wyatt, R.E.: Quantum interference within the complex quantum Hamilton–Jacobi formalism. *Ann. Phys.* **325**, 2193–2211 (2010)
63. Sanz, A.S., Borondo, F., Miret-Artés, S.: Role of quantum vortices in atomic scattering from single adsorbates. *Phys. Rev. B* **69**, 115413(1–5) (2004)
64. Sanz, A.S., Borondo, F., Miret-Artés, S.: Quantum trajectories in atom–surface scattering with single adsorbates: The role of quantum vortices. *J. Chem. Phys.* **120**, 8794–8806 (2004)
65. Chou, C.-C., Wyatt, R.E.: Computational method for the quantum Hamilton–Jacobi equation: One-dimensional scattering problems. *Phys. Rev. E* **74**, 066702(1–9) (2006)
66. Chou, C.-C., Wyatt, R.E.: Computational method for the quantum Hamilton–Jacobi equation: Bound states in one dimension. *J. Chem. Phys.* **125**, 174103(1–10) (2006)
67. Chou, C.-C., Wyatt, R.E.: Quantum trajectories in complex space. *Phys. Rev. A* **76**, 012115(1–14) (2007)
68. Goldfarb, Y., Degani, I., Tannor, D.J.: Bohmian mechanics with complex action: A new trajectory-based formulation of quantum mechanics. *J. Chem. Phys.* **125**, 231103(1–4) (2006)
69. Sanz, A.S., Miret-Artés, S.: Comment on “Bohmian mechanics with complex action: A new trajectory-based formulation of quantum mechanics” [*J. Chem. Phys.* **125**, 231103 (2006)]. *J. Chem. Phys.* **127**, 197101(1–3) (2007)
70. Goldfarb, Y., Degani, I., Tannor, D.J.: Response to “Comment on ‘Bohmian mechanics with complex action: A new trajectory-based formulation of quantum mechanics’” [*J. Chem. Phys.* **127**, 197101 (2007)]. *J. Chem. Phys.* **127**, 197102(1–3) (2007)
71. Yang, C.-D.: Quantum dynamics of hydrogen atom in complex space. *Ann. Phys.* **319**, 399–443 (2005)
72. Yang, C.-D.: Wave-particle duality in complex space. *Ann. Phys.* **319**, 444–470 (2005)
73. Yang, C.-D.: Modeling quantum harmonic oscillator in complex domain. *Chaos Solitons Fractals* **30**, 342–362 (2006)
74. Chou, C.-C., Wyatt, R.E.: Quantum vortices within the complex quantum Hamilton–Jacobi formalism. *J. Chem. Phys.* **128**, 234106(1–10) (2008)
75. Chou, C.-C., Wyatt, R.E.: Quantum streamlines within the complex quantum Hamilton–Jacobi formalism. *J. Chem. Phys.* **129**, 124113(1–12) (2008)
76. Needham, T.: *Visual Complex Analysis*. Oxford University Press, Oxford (1998)
77. Elmore, W.C., Heald, M.A.: *Physics of Waves*. Dover, New York (1985), Chap. 10
78. Guantes, R., Sanz, A.S., Margalef-Roig, J., Miret-Artés, S.: Atom–surface diffraction: A trajectory description. *Surf. Sci. Rep.* **53**, 199–330 (2004)
79. Gelabert, R., Giménez, X., Thoss, M., Wang, H., Miller, W.H.: Semiclassical description of diffraction and its quenching by the forward–backward version of the initial value representation. *J. Chem. Phys.* **114**, 2572–2579 (2001)
80. Zhang, S., Pollak, E.: Monte Carlo method for evaluating the quantum real time propagator. *Phys. Rev. Lett.* **91**, 190201(1–4) (2003)
81. Zhang, S., Pollak, E.: A prefactor free semiclassical initial value series representation of the propagator. *J. Chem. Phys.* **121**, 3384–3393 (2004)
82. Lopreore, C.L., Wyatt, R.E.: Quantum wave packet dynamics with trajectories. *Phys. Rev. Lett.* **82**, 5190–5193 (1999)
83. Walborn, S.P., Terra Cunha, M.O., Padua, S., Monken, C.H.: Double-slit quantum erasure. *Phys. Rev. A* **65**, 033818(1–6) (2002)
84. Tan, S.M., Walls, D.F.: Loss of coherence in interferometry. *Phys. Rev. A* **47**, 4663–4676 (1993)
85. Grisenti, R.E., Schöllkopf, W., Toennies, J.P., Hegerfeldt, G.C., Köhler, T.: Determination of atom–surface van der Waals potentials from transmission-grating diffraction intensities. *Phys. Rev. Lett.* **83**, 1755–1758 (1999)
86. Grisenti, R.E., Schöllkopf, W., Toennies, J.P., Manson, J.R., Savas, T.A., Smith, H.I.: He-atom diffraction from nanostructure transmission gratings: The role of imperfections. *Phys. Rev. A* **61**, 033608(1–15) (2000)

87. Omnès, R.: Consistent interpretations of quantum mechanics. *Rev. Mod. Phys.* **64**, 339–382 (1992)
88. Sanz, A.S., Bastiaans, M., Borondo, F.: Loss of coherence in double-slit diffraction experiments. *Phys. Rev. A* **71**, 042103(1–7) (2005)
89. Sanz, A.S., Borondo, F.: A quantum trajectory description of decoherence. *Eur. Phys. J. D* **44**, 319–326 (2007)
90. Dewdney, C.: Nonlocally correlated trajectories in two-particle quantum mechanics. *Found. Phys.* **18**, 867–886 (1988)
91. Lam, M.M., Dewdney, C.: Locality and nonlocality in correlated two-particle interferometry. *Phys. Lett. A* **150**, 127–135 (1990)
92. Dewdney, C., Malik, Z.: Angular-momentum measurement and nonlocality in Bohm’s interpretation of quantum mechanics. *Phys. Rev. A* **48**, 3513–3524 (1993)
93. Marchildon, L.: Two-particle interference devices and compatibility of Bohmian and standard quantum mechanics. *J. Mod. Opt.* **50**, 873–879 (2003)
94. Guay, E., Marchildon, L.: Two-particle interference in standard and Bohmian quantum mechanics. *J. Phys. A* **36**, 5617–5624 (2003)
95. Dürr, D., Goldstein, S., Zanghì, N.: Quantum equilibrium and the origin of the absolute uncertainty. *J. Stat. Phys.* **67**, 843–907 (1992)
96. Bacciagaluppi, G., Valentini, A.: *Quantum Theory at the Crossroads: Reconsidering the 1927 Solvay Conference*. Cambridge University Press, Cambridge (2009)
97. Norsen, T.: The theory of (exclusively) local beables. *Found. Phys.* **40**, 1858–1884 (2010)
98. Norsen, T.: Weak measurement and (Bohmian) conditional wave function. [arXiv:1305.2409v1](https://arxiv.org/abs/1305.2409v1) (2013)
99. Sanz, A.S., Borondo, F.: Contextuality, decoherence and quantum trajectories. *Chem. Phys. Lett.* **478**, 301–306 (2000)
100. Sanz, A.S., Martínez-Casado, R., Peñate-Rodríguez, H.C., Rojas-Lorenzo, G., Miret-Artés, S.: Dissipative Bohmian mechanics: A trajectory analysis of wave-packet dynamics in viscous media. [arXiv:1306.6607v1](https://arxiv.org/abs/1306.6607v1) (2013)
101. Ford, G.W., O’Connell, R.F.: Decoherence without dissipation. *Phys. Lett. A* **286**, 87–90 (2001)
102. Ford, G.W., Lewis, J.T., O’Connell, R.F.: Quantum measurement and decoherence. *Phys. Rev. A* **64**, 032101(1–4) (2001)
103. Ford, G.W., O’Connell, R.F.: Decoherence at zero temperature. *J. Opt. B, Quantum Semi-class. Opt.* **5**, S609–S612 (2003)

A Trajectory Description of Quantum Processes. II.

Applications

A Bohmian Perspective

Sanz, Á.S.; Miret-Artes, S.

2014, XIX, 333 p. 100 illus., 68 illus. in color., Softcover

ISBN: 978-3-642-17973-0